

Characterization of Self-Magnetic Pinch (SMP) radiographic diode performance on RITS-6 at Sandia National Laboratories: 1) Diode Dynamics, DC Heating to extend Radiation Pulse.

T. J. Renk, B. V. Oliver, M. L. Kiefer, T. J. Webb, J. J. Leckbee, M. D. Johnston, S. Simpson, and M. G. Mazarakis

Sandia National Laboratories, Albuquerque, NM 87185, USA

Corresponding Author: T. J. Renk, email: tjrenk@sandia.gov

ABSTRACT

Radiographic diodes focus an intense electron beam to a small spot size to minimize the source area of energetic photons for radiographic interrogation. The self-magnetic pinch (SMP) diode has been developed as such a source and operated as a load for the RITS-6 Inductive Voltage Adder (IVA) driver. While experiments support the generally accepted conclusion that a 1:1 aspect diode (cathode diameter equals anode-cathode gap) delivers optimum SMP performance, such experiments also show that reducing the cathode diameter, while reducing spot size, also results in reduced radiation dose, by as much as 50%, and degraded shot reproducibility. Analysis of the effective electron impingement angle on the anode converter with time made possible by a newly developed dose-rate array diagnostic indicates that fast-developing oscillations of the angle are correlated with early termination of the radiation pulse on many of the smaller-diameter SMP shots. This behavior as a function of relative cathode size persists through experiments with output voltages and currents up to 11.5 MV and 225 kA, respectively, and with spot sizes below \sim few mm. Since simulations to date have not predicted such oscillatory behavior, considerable discussion of the angle-behavior of SMP shots is made to lend credence to the inference. There is clear anecdotal evidence that DC heating of the SMP diode region leads to stabilization of this oscillatory behavior. This is the first of two papers on the performance of the SMP diode on the RITS-6 accelerator.

Key words: inductive voltage adder (IVA) accelerators, electron beam focusing, high-voltage techniques, magnetic insulation, impedance behavior in high-power anode-cathode (A-K) gaps, dose-rate diagnostics

I. INTRODUCTION

The Self-Magnetically Pinched (SMP) diode is a form of intense relativistic electron beam diode that was developed specifically as a potential x-ray source for short-pulse flash X-ray radiographic interrogation of dynamic experiments [1,2]. The conceptual basis of radiographic operation is depicted in Fig. 1. An electron beam is focused to as small a point as possible, in order to function as a point-source for x-ray interrogation of an object. The beam focuses on an anode composed of high-atomic-number material (e.g. tantalum), which results in an intense pulse of bremsstrahlung X-rays. The radiographic resolution is determined by the spot size of the x-ray source. The quality of imaging is affected by both x-ray energy (sets penetration ability) and x-ray fluence (sets illumination power).

The SMP diode is discussed in this paper as a diode load for the six-cavity Radiographic Integrated Test Stand (RITS-6) pulsed-power accelerator. The RITS-6 architecture is that of an Inductive Voltage Adder (IVA) feeding a magnetically insulated transmission line (MITL) [3]. In a MITL, the electric field strength at the negative electrode exceeds the threshold for electron emission, and the resultant self-insulated flow (behind an initial loss-front) represents current approaching the diode load over and above the current that is generated at the diode itself. The existence of MITL flow in an IVA leads to fundamentally different physics from that present in a vacuum line and high-voltage interface. In the latter, flow is not present. These flow electrons represent a complicating factor in characterizing the physics of the high-power diode fed by the IVA. The flow electrons occur separate from and in addition to currents flowing in the electrodes. The implications of IVA-MITL coupling will be discussed more later in the paper. SMP experiments on RITS have been performed at an output voltage from 3.5 to > 11 MV. For this paper, data discussion is focused in the voltage range from 4.5 to 8 MV.

The technology to form high-quality radiographic images using high energy electron beams was developed, starting in the 1960s, at what is now the Atomic Weapons Establishment (AWE) [4]. Additional development occurred at various other laboratories, such as France (Centre Etude Gramat) [5] and the United States (the Naval Research Laboratory (NRL) [6] and Sandia National Laboratories (SNL) [7], where RITS-6 is located). As accelerator technology advanced the driving voltage beyond 2 MV (typical), the drive pulse evolved from a vacuum feed into a high-voltage interface to a MITL fed by a multi-stage IVA. The flow electrons in a MITL represent a complicating factor in characterizing the physics of the high-power diode fed by the IVA. For this reason, in some experiment designs (including the RITS MITL and diode), hardware is added to divert the sheath flow away from the diode load [2,8]. In

the case of the RITS experiments described in this paper, the additional hardware will be fully described in Section II below. However, as the diode load ‘turns on’, and the diode current rises, the resultant magnetic field can steer the diverted current back towards the diode region. This is observed to happen in the RITS experiments discussed here, and can lead to significant implications for diode impedance behavior.

The theory of electron flow in large aspect ratio diodes, either without ions [9] or with ions included [10], was developed for diodes operated using a high-voltage interface, not an IVA. Experiments have been conducted using either a high-voltage interface [5] or IVAs as the driver. SMP behavior appears to be similar using either driver, but there is evidence from RITS experiments to be addressed in the second of these two papers that as the IVA impedance is raised beyond a certain point, the IVA-SMP diode system reacts in a fundamentally different way.

In an SMP diode operated in negative polarity (see Fig. 3), a cathode structure faces the anode side. The initial electron beam approaches the anode in a non-pinched manner. Then the rising current beam current deposits enough energy on the anode to heat and liberate ions from the anode. The source for these ions can be either monolayer contaminants on the surface that become ionized, or entrained ions in the atomic lattice of the anode. This occurs after the anode temperature has risen to some elevated temperature. Prior research [11] has suggested a threshold temperature of about 400°C as a thermal release point. These ions then counter-stream towards the cathode, and their presence helps neutralize the charge imbalance in the anode-cathode (A-K) gap. This in turn allows the electron beam to progress to a tight focus on the anode axis [10]. Simulations of current behavior in the RITS SMP diode using the hybrid particle-in-cell (PIC) fluid code LSP [12] confirm the formation of a tight beam pinch on the anode, occurring after about 10 nsec [13].

It is thus the presence of the counter-streaming ions that enables the electron beam to pinch down to a smaller spot size. The ion population can lead to complications in diode operation, however. The ions liberated by electron beam heating form a dense layer that expands away from the anode surface over time, like a similar expanding layer from the cathode side. The expansion of anode and cathode plasmas in the SMP diode, as in all high-power particle beam diodes, leads to a steady reduction in diode impedance as the power pulse progresses, due to the reduction in the effective A-K gap. If the expansion encompasses the entire distance across the A-K gap, this will lead to a premature impedance collapse of the diode. This point will be developed further in the experiment discussions below. One additional modification to the RITS SMP cathode resulted in a completely hollowed-out opening through the center

of the cathode, so as to allow for counterstreaming ions to transit and be detected within the field-shaper (see Fig. 3) [14]. Also, since the anode-plasma expansion region is greatest in the central pinch region, it is common practice to employ hollow annular cathode in an attempt to minimize the contact of the expanding anode plasma with the cathode [15].

The electron beam driving the SMP cathode fielded on RITS experiments is operated free from externally imposed magnetic fields. Since high currents are developed during the power pulse, it is possible that the beam could be subject to instabilities that could result in premature termination of the radiation and power pulse. Simulations using the LSP code have been undertaken by a number of research groups [5,16,17], including studies associated with the present paper [8,13,18,19]. Of the latter studies, a comprehensive description of simulations of the SMP geometry featured in this paper is given in Reference 19. In particular, the onset of abrupt and premature impedance collapse, an important behavioral factor addressed in the current work, is the subject of detailed LSP simulations using both 2D and 3D geometries. After previously determining that such collapses are unrelated to the pulsed power coming forward, sheath electron current in the transmission line, or accelerator hardware, the Reference 19 authors investigated the role of contaminants evolving from the anode surface, and variations in expansion rate of the dense anode and cathode plasmas evolving from their respective surfaces. The latter process is a common factor leading to decreasing diode impedance through the power pulse in high-power diodes, and is already mentioned above. Images of side-on framing camera images (not discussed in this paper) are compared for SMP shots with and without premature impedance collapse. Data are shown that correlate the appearance of such collapse with systematically higher anode and cathode plasma closure rates. But even with the higher closure rates listed, only a fraction of the 12mm A-K gap featured in the simulations could be closed within the 40 ns power pulse. The authors then posit the presence of less-dense plasmas below the level of diagnostic detection. The behavior of such subluminescent plasmas would apparently be difficult to distinguish between shots with and without premature impedance collapse. Radial nonuniformities in the anode plasma could possibly give rise to a larger v_r x B_θ acceleration into the A-K gap, but this requires either a pre-existing or evolving under-population of the on-axis anode plasma. Simulations duplicate the shape of the current increase associated with impedance collapse under this hypothesis, but not the rapidity of the increase seen in experiments. Several other observations, including the side-on framing camera analysis, could not distinguish between shots with and without premature impedance collapse.

Such previous attempts to predict impedance collapse from modeling of RITS SMP shots focus on the behavior of the cathode and anode plasmas. No mention is made of instabilities as a factor in SMP

impedance dynamics. Observations of instabilities in electrode plasma formation have been noted [5] that appear to produce asymmetries in focal spot behavior. More recent 3-D simulations [20] have been reported that make mention of both the resistive-wall and ion-hose instabilities. Both instabilities are shown to scale with either total or ion current in the diode. But the discussion centers on beam offset (that is, displacement of the beam center from the diode axis), not early termination of the radiation pulse, and the work is unpublished. Thus, the primary posited cause of shortened full-width-half-maximum (FWHM) radiation pulses in these previous studies is either partial or complete A-K gap closure due to the evolution of both cathode and anode plasmas away from their respective electrodes and towards each other [5,18,21].

At this point, it must be emphasized that any reduction in the typical 40-50 ns radiation pulsewidth in SMP diode experiments must be due to something other than the standard gap closure rate caused by converging anode and cathode dense plasmas in high-power diodes. As an example, consider a closure velocity of say ≤ 10 cm/ μ sec that can be considered typical in such diodes [5,19]. During a typical pulsewidth of 50 nsec, this amounts to at most a 5-mm closing of the A-K gap. But typical SMP diode A-K gaps [5, 7, 19, 21] are on the order of 8-12 mm, an amount significantly larger than the estimated gap closing due to the converging electrode plasmas. As already mentioned, this discrepancy is tacitly admitted to in the references cited, and explained by factors such as anomalous variations in the rate of electrode plasma expansion, or the effects of plasmas in the A-K gap less luminous (and less dense) than those of those of the observable anode and cathode plasmas, a speculative hypothesis not verified by experiment [19]. Interestingly, in the most recent comprehensive review of SMP experiments on RITS up to this point [7], it is stated that based on the relatively slow drop in impedance, the electrode plasmas do not significantly limit the diode operation in RITS SMP experiments.

The characterization of reduction in FWHM of the radiation pulsewidth, and mechanisms that may cause reductions, constitute a very important factor in the optimization of SMP diode performance. This is because of the results of scaling experiments more fully described below. In brief, for a given operating voltage, as the diameter of the SMP cathode is reduced, so does the resulting focal spot size. But as the cathode diameter is reduced, the tendency for the radiation pulse to be shortened increases. For example, in the RITS experiments conducted in the 7-8 MV output range, a cathode diameter of 12.5 mm, combined with an A-K gap of 12 mm (hereafter referred to as '12.5-12' geometry), resulted in very stable performance (~ 45 ns FWHM radiation pulse, > 300 Rads @ 1meter) over many shots and with any number of changes to the specific diode hardware (coatings, heating, etc.). And when the cathode diameter was decreased to 8.5 mm with a 8.3 mm A-K gap ('8.5-8.3'), the spot size was observed to

decrease. Similar scaling results have been reported elsewhere [5]. But in addition, the radiation FWHM on RITS is observed to decrease on as many as half the shots taken. FWHM can drop from a maximum of 35-40 ns to below 20 ns, and the radiation yield can drop by 50% or more. While a premature drop in radiation output is observed in experiments detailed in, for example [5], such an early termination occurred only in the case of the smallest A-K gap fielded, whereas this behavior is much more widespread in RITS data, as will be discussed.

This significant drop in radiation yield as well as dose reproducibility with cathode diameter reduction has significant implications for the use of the SMP diode as a reliable source for radiographic applications, since this implies that at least a factor two must be built into yield predictions. And although spot sizes for the same set of hardware dimensions tend to decrease as output voltage is increased, the possibility that cathode size may have to increase with facility size [18,22] may confer a built-in disadvantage.

It is thus imperative that effort is made to understand the reason for this tendency for shortened radiation FWHM to decrease significantly on many shots. If this trend could be mitigated or reversed, the payoff would be that a demonstrated mechanism for reduction of radiographic spot size, that of reduction with cathode radius, could be implemented with enhanced confidence in the shot-to-shot reproducibility of such diodes.

The remainder of this paper is organized as follows:

Section II: Description of the RITS hardware, experiment geometry, and diagnostics. A key diagnostic has been added compared with previous RITS experiments, a dose-rate monitor array [23] featured in a recent publication. Use of this monitor array allows for the inferring of the electron beam angle on the anode converter *as a function of time*, not just in the time-integrated aggregate. Qualitative and quantitative tracking of the electron angle yields evidence of fast-developing variations in electron angle that a) may indicate the presence of beam instabilities, and b) may provide a causal mechanism for the early termination of the radiation pulse due to impedance collapse. This may be key to explaining the difference in impedance behavior between the 12.5-12 and 8.5-8.3 SMP shots described above.

Section III. Description of the “baseline” behavior of both the 12.5-12 and 8.5-8.3 diode configurations already introduced above. This serves as a starting point in developing further the notion of a behavior suggestive of an instability-related early termination of the radiation pulse. Since a) there is no indication in simulations of SMP diode behavior of the presence of beam instabilities, and b) the behavior of the electron beam angle in an SMP diode as a function of time has not been previously investigated in

SMP experiments, it is important to establish a database for the description of SMP diode shots in terms of this angle variation. After such a characterization of beam angle behavior, the notion that the angle undergoes variations that can terminate the radiation pulse can then be offered as a competing narrative to the more commonly accepted electrode gap closure as the explanation of impedance collapse in SMP diodes.

Section IV. For this paper, the testbed for the development of an angle-based explanation of SMP diode behavior is a series of shots taken at the 4.5 MV output level, in which the A-K gap was varied from 3 mm to 11 mm. It is this wide range of A-K gaps that illustrates the variation in electron angle behaviors as a function of A-K gap. For these shots, the cathode diameter was fixed at 7 mm. Some 3 dozen shots were taken and are featured in this discussion. These were not the only RITS shots which featured a 7 mm cathode diameter and 4.5 MV output. A broader group of such shots is discussed in Reference 24. We focus on the smaller set here, because they were executed in a relatively short time span, with similar diagnostics fielded, and were specifically aimed at investigating the variation of A-K gap with fixed cathode diameter. Two notable results are noted here: a) as the A-K gap is raised, the radiation pulse FWHM and dose output are observed to increase up to a point, and the inferred beam angle on the converter decreases (i.e. impacts the converter at an angle more normal to the surface). This may be expected intuitively, and is in fact observed; and b) the less-expected result, and different from that observed in the Reference 24 experiments, is that the most variation in both dose output and radiation pulse FWHM are observed to occur, not at the smallest A-K gap, but at the gap (7 mm) most associated with the maximum in both dose and FWHM behavior. That is, the variation in performance of the 7-7 shots was the largest observed with the shot series. This does not appear to be consistent with the electrode gap closure explanation. In the course of investigating this behavior, we also confirm that the highest radiation dose occurs with the 7-7 configuration, thus confirming previous anecdotal observations [18,19,22] that the “1-1” aspect ratio (that is, where the cathode diameter and A-K gap are equal) offers the best SMP operating point.

Section V. Having established the basis for angle variation as a characteristic for SMP operation, we discuss the implementation of in-situ DC heating and RF discharge cleaning of the diode region with the goal of increasing the FWHM for the 8.5 – 8.3 shots, while maintaining that configuration’s lower spot size compared to the 12.5 – 12 configuration. While the data suggests that this was achieved, the number of shots taken is quite small, and further experiments are necessary to establish a statistical basis for this statement. Study of the ratio of PIN diode data for the 8.5 – 8.3 heated shots indicates that DC heating and/or RF discharge cleaning leads to a stabilization of the electron pinch angle, which appears able to extend the length of the radiation pulse.

In addition, an unexpected side-effect of the heating/cleaning experiments occurred. While it might be expected that the procedure would lead to increased diode impedance, because the inventory of contaminant ions was conclusively shown to be reduced, this did not in fact happen. Diode impedance in the 12.5-12 case actually decreased, and remained the same for the 8.5 – 8.3 configuration, this despite the observed increase in the FWHM in the latter shots. These behaviors can be better understood by viewing the SMP diode as one element of the IVA-SMP system. The initially diverted flow electrons described above are eventually drawn back into the diode region, and must be included as an integral part of the total interaction between the IVA and the diode load. A full discussion of this system view of the SMP diode as coupled to the driving IVA is the subject of the second of the two papers in this series.

Conclusions are left to **Section VI**. It is also noted that this paper is adapted and condensed from an extensive and comprehensive unpublished Report [25] of SMP experiments conducted on the RITS-6 accelerator. Reference to this Report will occur in the ensuing discussions below where appropriate in the interests of preserving a more compact and focused length of the present paper.

II. Description of RITS hardware, experiment geometry, and diagnostics

An overall simplified schematic diagram of the RITS-6 downstream MITL and load region is shown in Fig. 2. The MITL inner conductor (gray) is connected to the inductive voltage adder (IVA), out of view to the left. The MITL outer conductor is expanded into a much larger chamber that contains the inner MITL field shaper and load region. The large chamber shown, known as the ‘dustbin’, is fielded in several sizes, enabling a variation in voltage stress between the inner and outer MITL conductors. Near the point where the dustbin is attached to the outer MITL, the MITL inner conductor transitions to a conical structure (‘cone’), and then to the field shaper, or ‘knob’. The cone added to suppress dustbin resonances [8], believed to be caused by bursts of electrons with vortices at the entrance to the dustbin, and which are then shunted to the outer wall in discrete bunches. The function of the knob is to divert the MITL flow away from the A-K region. The cathode is fielded on the downstream end of the knob, opposite the anode/converter. The anode is shown penetrating the dustbin wall, so that supplementary hardware such as the DC heating system can be inserted through the dustbin wall. The red circle indicates that part of the drawing that is depicted in greater data, in Fig. 3. The red ‘Xs’ indicate the general position of Bdot current monitors that track the current flow towards the A-K gap. At the position marked ‘G’, just before the MITL outer conductor is attached to the dustbin, are a set of 4 equally spaced Bdots in azimuth on both the MITL inner and outer conductors. From this location, the voltage coming forward towards the A-

K region can be calculated using the theory of Miller and Mendel [26], as modified more recently [27, 28]. The form of the Mendel Equation used for this paper is given by an expression from Reference 27:

$$(1) \quad V = Z_0(I_a^2 - I_c^2)^{1/2} - [(gmc^2/2e) * (I_a^2 - I_c^2)/I_c^2]$$

where I_a denotes the total current measured at a particular point on the MITL outer conductor, I_c denotes the bound current at the same z-location on the MITL inner conductor, Z_0 is the MITL vacuum impedance of the MITL, and g is a parameter of order 1. (If g is set = 1, the original Mendel equation is recovered.) The value of g is determined from particle-in-cell (PIC) simulations, and for an output voltage of ~ 8 MV, g is determined to be ~ 0.8 . Accordingly, this value of g is assumed for the duration of this paper. In practical terms, the difference between a g value of 1 and 0.8 amounts to ~ 0.2 MV difference in the calculated voltage at the 8 MV level.

The method of calculation of the corrected diode voltage is the same as discussed in previous RITS papers [7], i.e. the corrected voltage (hereafter referred to as V_{CORR}) is calculated by inductively correcting the voltage at an upstream point where the voltage is determined from the Mendel formula:

$$(2) \quad V_{corr} = V_{MITL} - L_{dustbin} d[I_{diode}]/dt$$

where $L_{dustbin}$ is the estimated lumped-circuit inductance of the dustbin chamber. To determine the value of I_{diode} , we refer to the other three ‘Xs’ indicated in Figure 2. The first X, located near where the cone joins the field shaper, indicates where 4 equally spaced Bdots measure the feed (bound) current approaching the field shaper, a current we will refer to as I_{UP} since the current is measured upstream of the load region. The second X, located on the downstream side of the field shaper, denotes where 4 Bdots are located at 6.35 cm radius from the diode axis. These Bdots measure the current flowing through the cathode, and possibly through a limited region of possible faceplate emission. This current will be referred to as I_L , where L stands for Load. The current I_L will be used for the diode current in Eq. 2. It should be pointed out here that while Eq. 2 gives a mathematical prescription for calculating V_{CORR} , the formula contains several assumptions that may not be correct for the entire power pulse. V_{MITL} , for instance, is time-shifted to the diode position, typically by 7 ns, to approximately account for the transit time from the MITL position to the diode load. Voltages and currents at any point in a MITL (or conventional transmission line, for that matter) consist of a forward-going and return wave added together. In the lumped-circuit model described by Eq. 2, simply time-shifting a calculated voltage forward in time is likely to result in different return waveforms for the two respective axial positions. And V_{MITL} itself is determined from the

currents (through Eq. 1), which are assumed to be accurate at any time during the power pulse. However, as the discussion below will illustrate, V_{CORR} as given by Eq. 2 appears to be a reasonably accurate estimate, on the average, of the diode voltage.

The final X marks the position of 4 Bdots located at 11 cm radius off the diode axis on the anode side. The current measured here will be referred to as I_A , where A stands for the anode side. As will be seen in the next section, on a typical well-performing RITS SMP shot, I_{UP} tracks below the value of I_L until near the end of the power pulse. I_L is always less than the value of I_A . This is a clear indication that there is current flowing in the diode region outside of the A-K gap. The most likely source of this current is the initially diverted MITL flow, which is drawn towards the A-K gap once the diode current rises. We will discuss in more detail later our determination that on the vast majority of shots, the current that is the source of the diode radiation pulse is I_L , hence that is what is used in Eq. 2 above for the inductive correction. The enlarged vacuum chamber depicted in Fig. 2 has an estimated inductance of 330 nano-henrys. The value of L , however, contributes only as a second order effect. .

The MITL inner conductor depicted in Fig. 2 results in a MITL vacuum impedance of 51.3 ohms, and is referred to as the ‘Lo-Z MITL’. A reduced diameter inner conductor was also fielded on RITS for a number of shots. The vacuum impedance in that case was 102.8 ohms, and is referred to as the ‘Hi-Z MITL’. The Hi-Z MITL experiments were less thoroughly diagnosed (no streak imaging, for instance), and proved harder to analyze, than the Lo-Z MITL shots. Discussion of the Hi-Z MITL shots is addressed in the second paper of this series, which emphasizes the treatment of the SMP diode as driven by an IVA as requiring a coupled SMP-IVA “systems” approach. The remainder of this paper is concerned exclusively with the SMP diode driven by the ‘Lo-Z MITL’.

A close-up schematic view of the diode region is depicted in Fig. 3. The cathode at left is indicated to be partially hollow, and faces an anode that is considerably larger in diameter. (For later shots in which the ions emitted from the anode were characterized [14], the hollowed-out section traversed the entirety of the cathode length.) As indicated in the earlier discussion, the ‘standard’ aspect ratio for the SMP diode is 1:1, i.e. the A-K gap is approximately equal to the cathode outer diameter. For the ‘standard’ SMP geometry, a foil (usually of aluminum 10 microns in thickness) is suspended as a flat plane approximately 0.7 mm offset from the converter plate made of tantalum (Ta). The function of the foil was characterized in earlier experiments at AWE [29] as helping to mitigate impedance reduction due to plasmas evolving from the Ta surface. To the right of the Ta converter is additional aluminum in the form of circular plates (not shown) that act as a beam stop.

In experiments detailed later in this paper, the hardware was altered from this drawing to accommodate in-situ heating experiments. A current feed was installed at the right (not shown) to deliver DC heating current to the Ta converter plate, either with or without the foil in place. The cathode was drilled out so that the hollow profile extended through its entirety. In order to confirm that the ion inventory (primarily protons) originating at the anode was mostly or wholly removed by the heating, an activation foil diagnostic [14] as added to the left of the cathode (out of view). The cathode was then drilled out so that emitted ions could propagate through the center of the cathode.

Two additional diagnostic sets are not depicted in Fig. 2, and will be discussed here in some detail. The first is a set of three dose-rate monitors, P-I-N diodes mounted both unshielded and in shielded collimators, and fielded with accompanying TLDs mounted in proximity, allowing for absolute calibration of dose-rate. As mentioned in the Introduction, and described in more detail in References 23 and 25, a new feature of the analysis detailed in this paper is the use of the differing dose-rate scaling of these monitors with changes to the electron angle of impingement on the cathode, depending upon the angle of observation of those monitors with respect to the diode axis. A schematic drawing of the PIN diode array set as fielded is shown in Fig. 4. In this drawing, the labeling of the PIN diodes refers to the angle of observation with respect to the radiation source. Thus, the PIN located on the axial location with respect to the radiation source (0°), and located behind both a lead collimator and aluminum plate, is labeled PIN_0. The PIN located at the 45° observation angle is labeled PIN_45. In the 95° observation direction, there were two PINs fielded, one inside a tungsten collimator, and one fielded outside the same collimator. The PIN fielded inside the collimator is labeled PIN_95. To distinguish between collimated and uncollimated PINs at the same observation angle, we label the uncollimated PIN as PIN_95 (uncoll). This Figure also shows the materials located between the photon source and the PIN diodes. (In the case of both PIN_0 and PIN_45, the aluminum end flange of the vacuum chamber, which is in both their fields of view, is not shown for clarity.)

It is a well-accepted principle of radiation generation from electron beams impinging upon high-Z converters (e.g. tantalum) that the more oriented the average electron trajectory towards the axis (more normal to the converter the electron strikes), the larger the radiation yield. We introduce in the equations below the concept of the dose and dose-rate for radiation yield, but depart from the label for dose-rate used in References 23 and 25, to be more consistent with dose and dose-rate labels used in the more general literature. In place of D used in those previous references to stand for dose-rate, the term $D[\dot{\quad}]$ will be used instead, to allow for the use of D as the more common term for dose.

Thus, the dose-rate $D[\dot{\text{D}}]$ produced by electron impingement on the converter can be approximated by the following form:

$$(3) \quad D[\dot{\text{D}}] = cIV^x$$

where I = current in Amperes, V = electron energy in MeV, and c is a constant. The factor x (referred to as the x -factor) depends upon the electron beam angle of incidence, the details of the x-ray converter materials, and the angle of observation. The form of Eq. 3 is referred to generically as a Radiographer's Equation [30], and different forms have been developed by various researchers. Other forms of Eq. 3 have been proposed in the past. For instance, one traditional equation that dates from the 1960s and often referred to as the Martin equation [31-33] adds a decaying exponential in beam angle as well as beam voltage to the form of Eq. 3. Subsequent measurements [34] have demonstrated that the Martin formula deviates substantially from experimental data for angles greater than 15° . Almost all the angles discussed in this paper are significantly greater than 15° .

What all such Radiographer's Equations have in common is that the x -factor is assumed to be *fixed*, i.e. there is no provision for allowing the electron angle to vary as a function of time, which would cause the x -factor to vary in time. Operationally, dose-rate is normalized to total dose by comparison with the output of TLDs which accompany the dose-rate detector in close proximity. This means that any time-dependent variability of the x -factor is lost.

A different approach relies on the following empirical observation: the x -factor in IV^x scales not only with the average electron angle upon the converter, but with the angle of *observation* of a radiation detector such as a PIN diode. For example, the scaling of a PIN diode observing radiation output at or near the axis of the forward-radiation direction decreases in magnitude as the electron angle steepens (i.e. strikes at an angle more nearly parallel to the converter plane). But a similar PIN diode deployed at near-normal to the radiation axis does not scale this way. In that case, as the electron angle steepens, the PIN diode output *increases*.

This can be illustrated by describing the time-dependent dose-rate modeling method developed in Reference 23: Electrons comprising the RITS electron beam are posited to strike the RITS-6 converter package at both specific angles: $0^\circ - 80^\circ$ in 10-degree increments, and specific energies: 1-9 MeV in 1 MeV increments. The ITS -CYLTRAN code (cylindrical symmetry) [35] is then used to calculate photon spectra for each combination of electron angle and energy, for a total of 81 CYLTRAN calculations. (ITS

Version 3.0 is used for modeling in this paper.) Electrons that are backscattered from inside the tantalum anode are re-injected to mimic the effect of the diode electric field (also called “albedo suppression”). This artificial albedo suppression is required to ensure the electron’s energy is deposited in the converter package. It is assumed that the re-injection angle is unimportant since this angle will be randomized by the scattering events that result in the backscattering. Photon spectra are extracted in the 0-10°, 40-50°, and 90-100° polar angle bins (angle bins correlated with the three PIN locations). Mass attenuation/absorption coefficients are used to attenuate the spectra as appropriate for the intervening materials in each direction and calculate the dose-rate in CaF₂ (TLD material) for each of the three PIN detectors. These 27 datasets (9 electron angles and 3 observation directions) are then fit to dose-rate equations of the form:

$$(4) \quad D[\text{dot}]_N(\text{krad-cm}^2/\text{s/A}) = c_N * V_{\text{MODEL}}(\text{MV})^{x-N}$$

The “c_N” and “x_N” parameters for each detector direction (N = 0°, 45°, 95°) are listed in Table 1, which is reprinted from Reference 23. The fit assumes that D[dot]_N follows Eq. 3 for a large range of electron energies and electron angles. The accuracy of this assumption varies with individual angles and observation directions. This is described further in Reference 23, with the clear conclusion being that the use of IV^x scaling is a useful power-law approximation to the dose-rate data, as opposed to a precise law of physics. The term V_{MODEL} on the righthand side refers to the posited voltage values in the ITS calculations, not any experimentally-derived voltage.

Eq. 4 then constitutes a “Radiographer’s equation” that is specific to the RITS experiments when Table 1 values are used. Since dose-rate is a measured quantity for a given shot, Eq. 4 can be solved for a given posited diode voltage assuming a particular electron angle to the converter, given c, x, and the electron current. For this calculation, it is assumed that a constant percentage of the IBEAM current (15%) is composed of ion current, so IBEAM is multiplied by 0.85 to estimate the electron current. This is consistent with previous assumptions about the level of ion current on a typical RITS SMP shot [7]. Since Table 1 gives both c and x terms for a given assumed electron angle, the equation can be solved for a posited diode voltage V at that angle. These voltages can be compared with the diode voltage waveform, yielding an estimate for electron angle at a given voltage at a given point in time.

In practice, the PIN diodes in the 45° and 95° directions appeared to be affected by scattered photons within the RITS test cell, whereas the 0°-PIN appeared to scale accurately with the ITS-CYLTRAN modeling. The axial field of view towards PIN₀ and TLDs 1-4 (Fig. 4) is collimated by a small (3 cm-diameter) aperture in an otherwise large lead shield located approximately midway between the diode and

PIN_0, followed by a 2.5 cm-thick aluminum plate (in the later set of RITS shots) placed directly in front of the PIN. Evidently, this level of shielding from scattered photons is more successful compared to the other two directions. Comparison of the dose-rates measured by the PIN_95 and PIN_95 (uncoll) monitors show that while the waveshapes are almost identical, the uncollimated monitor gives approximately twice the amplitude as the collimated one. Since neither of the TLD sets associated with the 95° direction (see Fig. 4) are collimated, it is apparent that the TLDs in the 95° direction are exposed to both direct and scattered photons. This makes the dose that they measure higher than those predicted by the CYLTRAN modeling.

The net result is the following:

a) the behavior of the PIN_0 data appeared quantitatively as well as qualitatively consistent with the ITS-CYLTRAN modeling;

b) the PIN_0 data, added to the corrected voltage determined from the various current Bdots, can be combined with the qualitative PIN_45 and PIN_95 data to construct a self-consistent picture of the SMP electron beam pinch angle as a function of time. The effect of the scattered photons is that the PIN_95 detector magnitude appears to scale as $IV^{1.1}$ (compared to $\sim IV^{1.3}$ as in Table 1), and the PIN_45 detector magnitude appears to scale as $IV^{1.8}$ compared to $\sim IV^{2.5}$ as in Table 1. (In this statement, the ‘V’ is the experimentally derived voltage.) However, the *trend* of the x-factor behaviors for the PIN_45 and PIN_95 detectors appears to be correct. That is, for a shot in which the electron pinch angle on the converter, based upon the PIN_0 data, appears to be increasing in angle relative to the radiation axis (the PIN_0 magnitude is falling), the PIN_95 magnitude is rising at the same time, and the PIN_45 magnitude scales in a mixed way.

c) The additional dose-rate data from PIN_95 can be rendered quantitatively useful by making an assumption that the dose measured by the accompanying TLD next to PIN_95 be reduced by half, again as described in Reference 23. Comparisons with the same shot as analyzed with the additional corrected voltage data show approximately the same result, indicating that the factor 2 reduction in the TLD accompanying PIN_95 is roughly correct. But in this latter case, electron pinch angles and estimated corrected voltages can be determined by analysis of the PIN_0 and PIN_95 data alone, without the use of the corrected voltage data. This point is a very significant one. (The PIN_45 data continues to be used only for qualitative comparison.)

It is the behavior of the electron angle with time that will be used to infer the development of a (possibly fast-growing) oscillation in this pinch angle that can lead to premature termination of the radiation pulse.

We characterize a shot as indicating premature impedance collapse when the axial dose-rate PIN_0 signal terminates abruptly, usually well before the nominal end of the power pulse.

The second, and very important additional diagnostic is the time-resolved spot size diagnostic (TRSD). The development of this diagnostic is extensively detailed in Reference 36, and the TRSD was developed for use on the predecessor facility to RITS-6, RITS-3 [37]. A schematic drawing of the TRSD setup (top view) is depicted in Fig. 5, which is reprinted from Reference 32. In this Figure, photons emitted from the diode region propagate from *right* to *left*. They transit an aperture and impinge on a tungsten rolled edge. The TRSD itself consists of a one-dimensional array of 84 scintillating fibers (BC-20), each 250 μm in diameter and 80 mm in length, with temporal response of at least 3 ns. The fiber density is greatest in the middle of the array. In the second-generation version, the Image plate has been replaced by a scientific grade charge coupled device (CCD). By extracting penumbra information from the array produced by the rolled edge, the spot size and spot center can be determined as a function of time. Combined with the current measurements, the electron beam current density can in turn be derived. The image magnification can be varied by changing the first and/or second conjugate distances. The geometry is inherently one-dimensional, e.g. only information in the horizontal observation plane can be extracted. In the TRSD plots discussed in the next sections, there is an apparent jaggedness of the waveforms that is traceable to the discreteness in space of the fibers making up the TRSD. Also, the TRSD timing is connected to the current waveforms through a fiducial, but there is a ± 3 ns uncertainty in the TRSD timing with respect to the current waveforms.

In addition to the diagnostics described above, visual observation of the A-K gap was recorded with two different diagnostics: framing camera imaging, and streak camera imaging. Framing camera images are not discussed here. The streak camera hardware was developed by National Security Technologies (NSTec), and is described fully elsewhere [38]. A typical streak image from a RITS SMP shot is shown in Fig. 6. In this image, time proceeds from bottom to top, and cathode and anode location are noted as a function of the x-axis. The radiation pulse occurs in time within the horizontal pink dashed lines. In the false-color image, a luminous plasma is first generated from the anode side (red color indicating the most intense luminosity), and then from the cathode. The luminous plasmas from the respective electrodes are observed to approach each other (the triangular-shaped feature), then join together. The time of joining in this image occurs well past the end of the radiation pulse. Streak camera images from different shots are discussed in the various Sections below.

The combination of the current measurements, arrayed PIN diodes/TLDs, TRSD diagnostic, and streak cameras yield a comprehensive dataset, possibly the most comprehensive of any SMP experiment fielded. It is by combining information from these diagnostics that a self-consistent picture of SMP dynamics can be constructed. Details will be discussed below.

III. Characterization of ‘Baseline’ hardware at the 7-8 MV level: ‘12.5 – 12’ configuration. Change in performance as cathode is reduced in size: ‘8.5 – 8.3’.

We consider a typical well-performing SMP shot taken with the ‘12.5-12’ configuration, Shot 1908. In this case, the anode was an Al foil-over Ta, without in-situ heating. Referring now to the signals discussed in Section II above, a waveform plot including the currents I_A , I_L , and I_{UP} is shown in Fig. 7. Also shown is the (scaled) axial dose-rate given by PIN_0. In this plot, the I_L current is time-shifted +1 ns, and I_{UP} +7 ns, so that the currents display a simultaneous onset. The PIN_0 signal has also been time-shifted (-7.3 ns) to match the timing of the $IV^{2.1}$ waveform defined by V_{corr} and I_L . The behavior of the currents shown is typical of a stable, well-behaved RITS SMP shot. The I_A and I_L currents rise quickly, then continue to increase at a reduced rate. After rising together, the two currents split, with the difference between the two remaining almost constant for the rest of the power pulse. As previously mentioned, the difference in current reflects the influence of the initially diverted flow current, which then approaches in proximity to the I_A monitors, but not to the I_L monitors. The I_{UP} current lags behind the other two, then rises relatively quickly, almost reaching the level of I_L by the end of the power pulse. The difference between I_L and I_{UP} reflects forward-going current that is retrapped as bound current in between the two monitor locations (see Fig. 2). The PIN_0 dose-rate waveform is broad (reflecting the 47 ns FWHM of the radiation pulse), and relatively constant until it peaks at its end. The waveform sharp decrease coincides with the end of the power pulse.

The long-lived radiation pulse also reflects a relatively stable electron pinch angle behavior for this shot. To demonstrate this, we plot normalized waveforms in Fig. 8 for three dose-rate monitors, PIN_0 (axial), PIN_45, and PIN_95. The waveforms have been timeshifted to reflect their varied distances from the diode. The PIN_45 and PIN_95 waveforms appear almost identical in shape, except at the end of the pulse. The PIN_0 signal, on the other hand, remains relatively smaller in magnitude though most of the pulse, then rises sharply at the end. More importantly, at the same time that PIN_0 is increasing sharply, the PIN_95 is *dropping* in magnitude, while the PIN_45 signal remains high. The sharp increase in the PIN_0 signal, accompanied at the same time by a drop in the PIN_95 signal (see Table 1), points to a change in pinch angle of the electron beam, in this case a decrease in angle (i.e. more towards the

radiation axis). A full analysis [23] is consistent with an electron angle varying between 30° and 40° for the middle of the pulse, and then a decrease to below 20° for the sharp increase at the end. The x-factor in IV^x increases from 2.24 to 2.47 (Table 1) as the angle changes from 30 to 20 degrees, and the rise in PIN_0 reflects this increase in radiation dose.

We continue the Shot 1908 characterization by comparing its performance with a shot taken with the smaller ‘8.5-8.3’ configuration, Shot 1774. The anode had the same construction as 1908. A comparison of the I_A and I_L currents for the two shots is shown in Fig. 9. The 1774 current waveforms exhibit the clear indication of impedance collapse. That is, both I_A and I_L , after tracking their respective 1908 counterparts for a time, rise rapidly, while at the same time, the radiation pulse collapses. The other two waveforms are the *difference* between the 1908 and 1774 I_A and I_L waveforms, respectively. This difference is approximately the same for both shots. This implies that even though Shot 1774 suffers a premature impedance collapse, the amount of current flowing near but not through the A-K gap remains roughly equal to Shot 1908, where the impedance did not collapse. We introduce here the concept of the load or diode impedance. Since the I_L current is the presumed current flowing from cathode to anode, we define Z_{LOAD} as ratio of the corrected diode voltage V_{CORR_G} divided by I_L . Then a comparison of Z_{LOAD} for the two shots is shown in Fig. 10. (The bumps in the waveforms are ultimately describable to variations in the currents coming forward.) The 8.5–8.3 load impedance is observed to be slightly lower than for Shot 1908, and falls very slightly faster, until the impedance collapses. The difference in impedance is typical of the behavior of the RITS diode impedance data as a function of cathode radius, for the same output voltage, e.g. as the radius is reduced, the impedance is also reduced.

Data from the TRSD pertaining to spot size evolution for the two shots is shown in Fig. 11. Again, the behavior shown is typical of the difference in spot size variation in most of the 12.5-12 and 8.5 – 8.3 shots. The spot size on Shot 1908 is observed to drop quickly down to a minimum (correlated to the initial beam pinch), but then begin to grow after only a short time. The spot size in the 8.5-8.3 case (Shot 1774) drops to a lower value than for Shot 1908, and stays there for a relatively longer time, until the impedance collapse ends the pulse. This is quantitative evidence for what is discussed in the Introduction, e.g. when the cathode radius is reduced for a given output voltage, the spot size is observed to be reduced as well, but then the FWHM of the radiation pulse can be also reduced. The increase in spot size seen in Shot 1908 is predicted in the previous 3-D LSP simulations of SMP shots [19], and ascribed to a continuously growing beam emittance. We will suggest another mechanism for the increase in spot size below.

For an insight to the possible mechanism behind the 8.5 – 8.3 impedance collapse, we plot the normalized PIN signals from Shot 1774 from the three observation directions: axial, 45°, and 95°, in Fig. 12. Also plotted in the Figure is the (scaled) I_L current for the Shot (previously plotted in Fig. 9). The behavior of the three PINs should be compared to that of the same three PINs on Shot 1908 (Fig. 8). This Figure is plotted in units of ns to better illustrate the timing differences between the waveforms. In the previous shot (1908), the axial PIN (PIN_0) was observed to peak at the end of its pulse, even as PIN_95 falls. In Shot 1774, PIN_0 also peaks as PIN_95 falls, but the behavior has some key differences. Whereas the PIN_95 waveform never recovers after its peak in Shot 1908, in Shot 1774 PIN_95 reaches its maximum well after the peak in the PIN_0 signal (>10 nsec later, in fact). And it is the fall of PIN_95, not that of PIN_0, that is correlated to the sharp increase in the IBEAM current. A close examination of the timing indicates that the three PIN signals begin to deviate in time at 2307 ns (onset of angle change), whereas the load current I_L begins its abrupt inflection upward at 2319 ns, about 12 ns later. Thus, whether or not the onset of angle change is the cause of the premature impedance collapse seen on this shot, the onset clearly occurs before the collapse starts.

A Radiographic unfold for this shot indicates that the beam pinch angle for 1774 is relatively stable at 30° up to the point of the PIN_0 spike, where the beam angle drops to 20°. The spike maximizes the dose-rate (it is actually higher than the maximum PIN_0 dose-rate for Shot 1908). The fact that on many of the 8.5 – 8.3 shots, the PIN_0 dose-rate peaks higher for the shots exhibiting premature impedance collapse is evidence for a momentary beam ‘straightening’ (e.g. smaller-angle with respect to the radiation axis). This is then followed by a sudden drop in dose-rate relative to the side-on PIN_95 monitor, e.g. the beam appears to turn inward. This behavior is very suggestive of some beam-generated change in electron angle and related to some kind of unstable behavior. A comparison of the PIN_0 waveform in Fig. 12 with the 1774_spot size waveform in Fig. 11 indicates that PIN_0 peaks at approximately just before the spot size begins its rise, signaling the impedance collapse in Shot 1774.

The preceding discussion of the behavior of the Shot 1774 PINs gives anecdotal evidence that some kind of behavior suggestive of a pinch instability terminated the radiation pulse. The discussion is anecdotal because up to this point, there have been no simulation of SMP diode behavior that predicts such an instability. One possible cause may be connected to the observed higher levels of current density in the 8.5 – 8.3 diode (as measured by TRSD), as much as 50% higher. In the remainder of this paper, additional evidence is presented of this behavior in the PIN diode signals occurring preferentially in shots with reduced FWHM. Also, when considering other mechanisms of premature impedance collapse, additional anecdotal evidence will be presented which argues against another hypothesized mechanism of such a

collapse, that of closure of the diode A-K gap plasmas [21]. Such evidence is presented in some detail in the following section, which discusses a series of RITS shots in which the A-K gap was varied.

IV. Study of pinch angle variation with variation in A-K gap at 4.5 MV output.

As an example of pinch angle characterization, we present a series of 33 shots was taken at the 4.5 MV output level, in which the primary purpose was to characterize variations in performance as the A-K gap was varied. All shots featured a cathode of 7 mm diameter. The gap was varied from a minimum of 3 mm to a maximum of 11 mm. A plot of the radiation dose for the shot series is shown in Fig. 13. The radiation dose (normalized to 1-meter distance (CF_2)) is observed to vary significantly, by almost a factor 6, over this A-K gap range. The shots are listed using the earlier stated convention, i.e. a 7 mm cathode and 3 mm A-K gap is written as “7-3”, and so on. A similar plot of time-integrated PIN_0 (axial) signals would look very much the same. That is, the ratio of TLDs to time-integrated PIN_0 is almost constant. This shows that TLD and time-integrated PIN_0 measurements behave consistently across the spectrum of shots. The maximal envelope of the output rises to a peak for the 7-8 shots, and then declines. Part of the explanation for this is ascribable to the variation in load voltage and current over the A-K gap range, but there is a second factor. The angle at which the electron beam approaches the converter also changes, and this leads to an increase in dose, as will be discussed below. Equally notable is the variation in dose output at the same A-K gap, particularly with the shots with 6 mm and 7 mm gaps, where the variation in output is approximately a factor of 3. This difference is much greater than that seen at either larger gaps (8 and 9 mm gaps) or smaller gaps (3 mm and 4mm). Thus what might be expected to be a stable operating point (7 mm, analogous to the stable 12.5-12 diode at higher voltage) exhibits significant dose (and FWHM) variation. The goal of this section is to study further both the overall dose variation (maximal envelope), and the apparently unstable behavior of the 7-7 shots (and to a lesser degree, the 7-6 shots).

A plot of the peak PIN_0 dose-rates from the same dataset as Fig. 13 is shown in Fig. 14a. While the outer envelope looks very similar to maximal values in Fig. 13, the lower-value points away from the outer envelope are missing. This occurs because of the following two factors: 1) the peak in PIN_0 is generally reached early in the power-pulse, so small and large FWHM shots can have almost the same peak dose-rate, and 2) in a significant number of cases, shots with premature impedance collapse often show a higher peak dose-rate than shots with a full radiation pulse. More will be said about this point later in this paper. A companion plot to Fig. 14a, showing peak dose-rates for the off-axis PIN_95, is shown in Fig. 14b. This is clearly a dataset with a very different behavior than for the axial PIN_0 signals. For instance, the two peak values for PIN_95 for the 7-3 shots are equal to the values for the 7-7 and 7-8

shots. Fig. 14b reinforces the discussion in Section II (and Table 1), that the off-axis PIN₉₅ detector behaves in a manner opposite to that of PIN₀ as the electron angle on the converter changes.

Study of “successful” shots. Comparison of Figs 13 and 14a suggests that further analysis might discern underlying trends better if the shots with full or near-full radiation pulse (termed “successful” shots) are separated from shots with premature impedance collapse (termed “unsuccessful” shots). Accordingly, a subset of “successful” shots is chosen for further study. The RITS numbering for these shots are as follows: 3 mm – 1552, 4 mm – 1549, 5 mm – 1548, 6 mm – 1541, 7 mm – 1537, 8 mm – 1556, 9 mm – 1558, and 10 mm – 1563. Both 11 mm shots suffered rapid impedance collapse and are not included here. The 3 and 4 mm shots have shortened FWHMs, attributable to evident early gap closure due to their small gap size. Streak camera images for those shots clearly show visible electrode plasmas approaching in close proximity within the time of the power pulse. Radiation dose @ 1 meter for the listed shots is shown in Fig. 15a. While the dotted curve has the smooth appearance of computer simulation output, the data are experimentally derived.

The effect of the electron pinch angle on the dose is illustrated in Fig. 15b. The data here are derived from CYLTRAN voltage unfolds using the PIN₀, ₄₅, and ₉₅ waveforms [23]. For the two 3 mm shots taken, the inferred average initial electron pinch angle is 60 degrees. This is not surprising, since with such a small A-K gap, the electrons must pinch in severely to reach the anode axis. For the two 4 mm shots, this angle is 50 degrees, then falls to 40 degrees and below as the A-K gap is increased. For almost all the shots at 6mm gap and above, the inferred initial electron angle is either 10 or 20 degrees. This change in angle makes a large difference in the radiation output produced in the axial direction (PIN₀). Consider the difference between a 60 degree and 10 degree electron angle, for a power pulse of average voltage 4 MV and average current 100 kA. The CYLTRAN unfold for a 60-degree angle yields an x-factor of 2.11, whereas for 10 degrees, x is 2.67 (x-factor values taken from Table 1). Then the difference in dose between an $IV^{2.11}$ and $IV^{2.67}$ pulse is greater than a factor 2, e.g. a 10-degree pinch produces twice the radiation output as a 60-degree pinch. This contributes to the steep rise in dose as the A-K gap is increased.

Beyond 8 mm A-K gap size, the dose decreases because the load voltage reaches a plateau, but the load current decreases as the A-K gap is further increased (higher impedance), leading to the drop in dose.

The behavior of the dose data in Fig. 15a reinforces anecdotal observations that SMP performance is optimized at an aspect ratio of approximately 1:1. There is another reason for this aspect ratio choice that

can be gleaned from RITS SMP data. As the A-K gap is increased, the measured spot size (not shown) also increases, gradually at first, then significantly above 8 mm A-K gap. A possible reason for this spot size increase is discussed below.

The behavior of Z_{LOAD} for this restricted shot set is shown in Fig. 16, plotted as a function of A-K gap. As in many of the plots based upon current, the waveforms are filtered to smooth out variations caused by both rapid and small variations in averaged current at the various monitors, and the effect of dustbin ‘resonances’ on the currents. The resonances cause ringing in the current waveforms which increase as the A-K gap is increased. The Z_{LOAD} magnitude is observed to increase steadily as the A-K gap is raised. The slope of the impedance fall (dZ/dt) varies within each A-K gap group, but in general, decreases as the gap is increased. For a 3 mm A-K gap, the initial diode impedance barely exceeds 30 ohms, which is significantly undermatched to the MITL impedance. The initial diode impedance for Shot 1556 (and for the larger A-G gaps) exceeds 60 ohms. Since the flow impedance of the Low-Z MITL used in these experiments is approximately 40 ohms, a tentative conclusion can be made that to eliminate the retrapping wave caused by undermatching to the load, at least for the duration of the power pulse, the diode impedance (at least initially) must exceed 1.5 times the MITL flow impedance.

We consider two of the ‘successful’ shots for further discussion: 1) Shot 1540, featuring a 7-6 configuration, and 2) Shot 1558 (7-9). Load currents (I_L) are shown for the two shots in Fig. 17a. (The additional waveform, (scaled) spot size from TRSD as a function of time for Shot 1558, will be discussed below.) These shots are chosen because they display aspects of SMP diode dynamics between shots with $< 1:1$ aspect ratio (A-K gap less than cathode diameter) and shots with $> 1:1$ aspect ratio. Neither of these shots appears to suffer beam instabilities or premature impedance collapse. The axial PIN_0 signals are shown in Fig. 17b. The FWHM in Shot 1540 is shorter than Shot 1558 (41 compared to 49 nsec). The most notable difference, however, is that the 7-6 PIN_0 peaks very early in the pulse, then falls continuously, whereas the 7-9 PIN_0 grows steadily through most of the power pulse. The respective behavior of the spot size with time, shown in Fig. 17c, is also observed to be quite different. In the 7-6 case, spot size falls slowly throughout the pulse until near its end. By contrast, the 7-9 spot size reaches its minimum early in the power pulse, and then almost immediately begins to rise. There are aspects of this difference that parallel the comparison between the 12.5 – 12 and 8.5 - 8.3 configurations at 7-8 MV output voltage, as discussed in Section III above. Fig. 17c should be compared to Fig. 11. In that earlier Figure, the spot size with time for the smaller 8.5 – 8.3 configuration (Shot 1774) reaches a lower value compared to Shot 1908. (The size then rises quite soon due to the premature impedance collapse on this shot.) By contrast, the spot size waveform for Shot 1908 reaches a minimum early in the pulse, then starts

to rise relatively sooner thereafter, much like the 7-9 spot size behavior in Fig. 17c. In the two respective shot pairings, the 12.5-12 and 7-9 configurations would be considered the ‘stable’ performers (e.g. no premature impedance collapses), while the 7-6 and 8.5 – 8.3 configurations can both suffer such collapses at their respective output voltages. The behavior discussed here is not limited to these few shots. That is, falling dose-rates and relatively stable spot sizes are observed together in any number of RITS shots. The question can then be asked if the behavior of the dose-rate and spot size are unrelated features of SMP diode dynamics, or are coupled in a causal way.

The CYLTRAN-based unfold of electron pinch angle for these two shots is as follows: a) for Shot 1540 (7-6), the pinch angle starts at 20 degrees ($IV^{2.47}$), then steepens to 40 degrees ($IV^{2.24}$) – see Reference 23 for further discussion; b) for Shot 1558, the pinch angle also starts at 20 degrees, then decreases to 10 degrees for a time, then ends at 20 degrees. This suggests the possibility that it is the steepening of the electron pinch towards the radiation axis that maintains small spot size, whereas it is the ‘straightening’ of the pinch, e.g. reduction of the pinch angle, for ‘stable’ shots, that contributes to the growth in spot size. However, a conclusive determination would require systematic study that is outside the scope of this paper. The principal conclusion that appears valid at this level of investigation is that the various aspects of SMP performance – spot size, pinch current density, FWHM behavior – may indeed be linked, and ultimately ascribable to systematic variations in electron beam optics in the A-K gap.

There is another aspect of SMP diode dynamics that is illustrated by the third waveform plotted in Fig. 17a. The first two I_L waveforms for Shot 1540 (7-6) and 1558 (7-9) are observed to undergo a similar qualitative behavior: after a rapid initial rise, the slope dI/dt of the rise decreases to a perceptively lower value (at \sim time = 2.28 μ sec). The rise then remains constant at this lower value until the end of the respective power pulses. The third waveform in Fig. 17a, the (scaled) spot size with time from the TRSD diagnostic for Shot 1558, indicates the probable cause for this current inflection. Near the point where the spot size reaches its minimum, the fast electron in-pinch enabled by the emitted ion current is complete, and the beam impedance evolves to a higher-impedance load line. The relative timing of the spot size for the other Shot, 1540 (Fig 17c), shows a similar behavior. Recall that in the earlier theoretical study of the RITS SMP diode [19], 3D PIC simulations predict an immediate increase in spot size ascribed to continuously growing beam emittance. (The 2D simulations undertaken at the same time do not predict such a spot size increase.) Evidence for such an emittance growth may be seen in the behavior of the Shot 1558 spot size. Reference 19 does not state the A-K gap chosen for the 3D simulations predicting spot size growth. A simulation of the Shot 1540 configuration (7-6) likely would not indicate emittance

growth. This change in current increase coincident with the completion of the beam in-pinch (or the lack of it) is discussed below in connection with the ‘unsuccessful’ shots.

Study of “unsuccessful” shots. We now switch the focus to the “unsuccessful” shots as described above, i.e. shots with premature impedance collapse as manifested by a truncated radiation pulse. Evidence in the RITS dataset for premature impedance collapse occurs principally in three places: 1) a sudden rise in both the I_L and I_A waveforms, usually accompanied by 2) a sharp fall in the axial PIN_0 dose-rate monitor; and 3) the appearance of a large retrapping wave at current locations located in the upstream MITL well away from the diode load. An analysis is made of all three waveforms in a prior study [24] of RITS shots taken at the 4.5 MV output level, which primarily focused on shots not included in the present study. That being said, it is our view here that a complete study of such ‘unsuccessful’ shots lies outside the scope of the present paper, due to the complexity of the topic, and the relative lack of causal evidence for the onset of premature impedance collapse. We give only a brief overview here.

One such example of the complexity can be seen by going back to Fig. 17a, the discussion of which points up a change to the current rise (inflection) occurring at $\sim 2.8 \mu\text{s}$. In a number of the ‘unsuccessful’ shots studies here, the current inflection point simply does not happen, i.e. the initial current rate of rise continues. The radiation pulse in the case of the fast-rising currents terminates at the point where the I_L currents separate from the currents which transition to the lower dI/dt on the other shots. While this lack of current inflection change tends to happen on shots with smaller A-K gap, the inflection change *does* occur on the shots with the smallest A-K gap, 3 mm (Shots 1551 and 1552). The behavior described in Reference 24 is limited to shots in which the transition to slower current rate-of-rise does in fact occur. This points to at least two different mechanisms responsible for premature impedance collapse, one occurring for shots in which the transition to lower slope occurs, and one occurring where the transition does NOT occur.

Diagnostic data from the streak camera diagnostic present an incomplete picture of the collapse process and mechanism. Images from the streak camera diagnostic exist in almost all the shots discussed. In these images, the luminous anode and cathode electrode plasmas are observed to converge together at different rates depending upon the shot, but typically the cathode plasma expands faster than the anode plasma. For the smaller A-K gaps (7-3 and 7-4), the luminous plasmas are observed to come together at a streak time consistent with the time of radiation pulse collapse. It can be inferred then that the mechanism of collapse is directly related to gap closure caused by the electrode plasmas intersecting. For both 7-3 shots, IBEAM

risers rapidly, and even though the transition to lower dI/dt occurs, the load voltage is heavily weighted down by the low diode impedance (Fig. 16), which for Shot 1552 barely exceeds 30 ohms.

However, for gaps of 5 mm and larger, the streak images do not show the luminous plasmas to join at the time of impedance collapse. In most of the shots, the luminous plasmas are observed to join at least 60 ns and usually closer to 100 ns after the start of the IBEAM current. In some to the 7-5 and 7-6 shots, it could be argued that these numbers are consistent with some of the shots in which both initial decreased then increased dI/dt occurs. But as has been pointed out above, for the shots in which the initial decreased dI/dt does not occur, the time to impedance collapse is as little as 35 ns, which is clearly too short compared to the closure times mentioned above. And for shots with cathode diameters of 7 mm and above, the luminous plasmas are nowhere near joining when the typical impedance collapse occurs, if it occurs.

As an example of the uncertainty in the analysis of premature impedance collapse presented by the 4.5 MV shots, waveforms from two shots in that series (1559 and 1536), taken with the 7-7 configuration, are presented in Fig. 18. The load currents I_L are shown, along with (scaled) axial dose-rate signals (PIN_0) for the two shots. One of these shots (1536) clearly shows the onset of impedance collapse, and the other does not. Yet prior to that collapse (at $\sim 2.3 \mu\text{s}$), the two sets of waveforms look virtually identical. The most significant difference appears in the 1536_PIN_0 signals, which prior to its collapse shows some oscillations the magnitude of which appears bigger than that in 1559_PIN_0. A plot of normalized signals from the PIN_0 and PIN_95 PINs (not shown) displays the same indication of fast angle change indicated in Fig. 12 for Shot 1774 (PIN_45 was not yet deployed when the 4.5 MV shots were taken). And a check of similar normalized PIN_0 – PIN-95 comparisons of the other 7-7 shots which undergo impedance collapse indicates that in virtually every case, the behavior shown in Fig. 12 occurs, i.e. asymmetrical behavior of the two PIN signals. This builds a strong anecdotal case that some kind of rapid angle change occurs which results in the termination of the radiation pulse.

Further evidence for this behavior is presented in Figs. 19a-c. The data shown here are from Shot 1774, the Shot featured in Fig. 12. Again, the 4.5 MV A-K gap shots discussed in this section were taken before the installation of the PIN_45 monitor signal shown in Fig. 19a. Figure 19a shows the (normalized) waveforms for the three PIN monitors. The fourth waveform is derived using the PIN array angle analysis [23], and shows the electron beam pinch angle (GREEN) as a function of time. It is observed that a) PIN_0 reaches a peak ~ 10 ns before PIN_45 and PIN_95 reach their respective peaks, as already pointed out in the discussion of Fig. 12; and b) the timing of the PIN_0 peak matches the time when the pinch

angle reaches its minimum ($2.31\mu\text{s}$), after which the angle increases quickly. The path of the pinch angle evolution over time can be depicted in what may be termed $D_0 - D_{95}$ space [23], where time is indicated only implicitly. This is shown in Fig. 19b. In this Figure, the D_0 and D_{95} labels refer to the absolute dose-rate at the PINs in the axial and 95° direction, respectively, where the data are normalized to remove the distance and specific electron current.

The RED points indicate time before the PIN_0 peak seen in Fig. 19a, and the BLACK points after. It appears that the beam pinch angle is mostly concentrated in the 30° - 40° region of the angle contours, but at one spot, the angle reaches 20° , the peak of the PIN_0 signal (RED changes to BLACK). Thus, the reason for the peak in PIN_0 is connected with the minimization of the pinch angle (beam goes straighter), and thus reaches a local maximum in IV^x . This also explains the time asymmetry between the PIN_0 and PIN_{45} - PIN_{95} signals. Since the radiation dose-rate collapses very soon after this point, one may infer an oscillation in the beam angle which could have contributed to the radiation pulse termination. Fig 19c shows the electron beam pinch angle (GREEN curve in Fig. 19a) plotted with the 1774_spot size waveform (the latter also shown in Fig. 11). The comparison shows that as the angle fluctuates prior to its final drop, the spot size remains relatively constant during this time. Fig. 19c is notable in that, unlike Figs. 19a and b, which only contain PIN waveforms or plots derived from them, the waveforms compared in Fig 19c are derived from completely different diagnostics (PINs vs TRSD). This further lends credence to this picture of pinch angle behavior.

Behavior of this kind provided by the PIN monitors provide strong anecdotal evidence that the reason for the observed impedance collapse is casually connected with some kind of unstable behavior leading to the collapse. The data presented here are connected primarily with the second described Z-collapse, namely that for which both the initial decreased dI/dt and later increased dI/dt occur. This implies that the ion beam-initiated strong electron pinch occurs, allowing for small radiographic spot size to occur, but then some later mechanism terminates the radiation pulse. The first described collapse, in which the initial reduced dI/dt does not occur, may be ascribed to a different process.

While the amount of anecdotal evidence for a pinch instability mechanism is large, such evidence is not definitive. As previously mentioned, no evidence of such an instability has occurred in the rather extensive modeling of SMP diode behavior that has already been undertaken. A stronger case for such a mechanism is outside the scope of this paper, and would be the subject of future work. In the meantime, this investigation has resulted in an accumulation of evidence arguing against the electrode plasma

closure explanation (19, 24) as the dominant mechanism for premature impedance collapse. The evidence can be summarized as follows:

- 1) One proposed differentiating argument for ‘successful’ and ‘unsuccessful’ shots like the 7-7 shots described above (Fig 18c), is that there is a variation in the rate at which the electrode plasmas approach each other. If in fact the electrode plasmas were to follow different closing velocities, then the effective impedances for different closure rate would follow different load lines. This in fact is observed to happen for the shots in which there is no initial transition to reduced dI/dt . But for the 7-7 shots described above (and more extensively in Reference 24), this does not apply, as *all* of the 7-7 shots undergo the initial reduction in dI/dt . That is, the 7-7 IBEAM waveforms for both ‘successful’ (e.g. larger FWHMs) and ‘unsuccessful’ e.g. smaller FWHMs) follow the *same* load line prior to the impedance collapse of the ‘unsuccessful’ shot. This is shown for example in Fig. 18. This is not consistent with shots in which electrode plasmas are converging towards each other at different rates, since in those shots, the respective load lines would diverge relatively early in time.
- 2) As previously mentioned, the lack of indicated closure of the luminous plasmas for A-K gaps larger than 4 mm has been previously explained [19] by positing that there are plasmas present at densities below the level of detectability by the available diagnostics, but with densities sufficient to interfere with and terminate the radiation pulse prematurely. As has already been pointed out earlier, it is not clear how the dynamics of a non-detectible low-level plasma can be compared between shots with and without impedance collapse. But it should also be pointed out, that if in fact, such ‘subluminous’ plasmas were present on all shots, their presence should lead to rapid impedance collapse on *all* the small AK gap shots. The radiation FWHMs for the 4.5 MV shots discussed in this Section are shown in Fig. 20. The smallest observed FWHMs (excepting the 7-10 and 7-11 shots) are associated with the 7-5, 7-6, and 7-7 shots, all of which have shots with FWHMs lower than either the 7-3 or 7-4 shots. In particular, the FWHMs for the 7-7 shots range from 17 to 52 ns, a factor 3 variation. The effect of such ‘subluminous’ plasmas must then be very selective.
- 3) In both References 19 and 24, the characterization of ‘successful’ and ‘unsuccessful’ shots includes a waveform comparison of the axial PIN₀ dose-rate monitor with the load current I_L . That is, it is observed that the collapse of the radiation pulse as characterized by the rapid fall in the PIN₀ waveform is correlated with the abrupt rise in diode current that signals a premature

impedance collapse. But there are two observations concerning the PIN₀ waveform that considerably complicate this picture: a) on a significant number of such ‘unsuccessful’ shots, the PIN₉₅ signal lasts much longer than the PIN₀ signal, as much as 10 to 15 ns after PIN₀ collapses (see, for example, Fig. 12); and b) as described on 7-7 shots in particular, the PIN₀ waveform on even relatively good FWHM shots (30 to 40 ns), peaks much earlier than the PIN₉₅ waveform. Even as the PIN₀ waveform does not collapse, e.g. drop very quickly after peak, it declines considerably after peak, even as the PIN₉₅ magnitude holds steady or even rises. In all these cases, the fall in PIN₀ is not correlated with any rapid rise in the I_L waveform. Thus, in these cases, the behavior of PIN₀ correlated with I_L cannot be used to characterize a ‘bad’ shot.

- 4) And finally, there is one compelling anecdotal observation. There was in fact one shot taken (Shot 1910, standard 12.5 – 12), in which the forward-going pulsed power suffered a fault. An early-firing switch resulted in *two* power pulses timed ~ 150 ns apart. The result was two radiation pulses, of almost identical dose-rate, as seen with the PIN₉₅ waveforms in Fig. 21. Since the diode voltage dropped considerably from a normal shot, the dose-rate of the two pulses was significantly lower than average. Of course, there is no information diagnostically available as to the conditions in the diode at the time of the second pulse, but one can imagine that there could be high levels of residual plasma present in the diode region. This suggests that the SMP diode is rather robust in its operation. If it can survive such a condition and operate again within a span of 150 ns, this negatively impacts the hypothesis of the ‘subluminous’ plasma presence as leading to a diode short.

Another conclusion of this 4.5 MV A-K gap study is a hypothesis as to why the 7-7 series at 4.5 MV, taken as a whole, does not demonstrate the kind of stability exhibited by the 12.5-12 shots taken at the 7-8 MV level. The radiation dose-rate of a typical 7-7 shot, described by PIN₀, more closely resembles the dose-rate of an 8.5 – 8.3 shot than a 12.5 – 12 shot. The behavior of the spot size also more closely resembles that of a typical 8.5 – 8.3 configuration shot. This suggest that a more “ideal” 1:1 configuration for the 4.5 MV level on RITS-6 would feature a larger cathode diameter, like an 8-8 or even 9-9 configuration.

V. In-situ DC heating and RF discharge cleaning of the load region and its possible stabilization of the electron beam pinch angle variation.

Implementation of either in-situ heating, or RF discharge cleaning, or both, have become standard tools for reducing contaminant inventories in any number of research facilities. It is important to distinguish at this point between two separate questions connected with heating/cleaning techniques:

- 1) Did the heating/cleaning procedure implemented lead to a validation of the expected reduction in contaminant inventories in the diode region, and
- 2) If so, did the reduction have an effect (positive, it is hoped) on diode operation?

Investigation of these two questions usually involves separate experimental studies (as is the case here). For any heating/cleaning protocol to be considered successful, data indicating an affirmative answer to both questions should be a minimum requirement. We discuss here the techniques and hardware for the heating/cleaning, but in a relatively brief way. This is so for two reasons: 1) A more comprehensive description of the complex issues involved in DC heating and RF discharge cleaning is planned for a future publication; and 2) while we believe that these techniques led to a successful outcome, that conclusion is based upon a relative handful of shots. A more thorough evaluation would be the subject of future experiments.

VI. DC heating. We first discuss the development of the DC heating approach. Two types of DC heating were operated on RITS-6, a long-time scale method in which DC heating current is delivered in close proximity to the anode, and a pulsed heating approach in which fast-response batteries deliver current to heat the Ta anode above 2500°C in approximately 1 second. The latter approach was originally developed at the Naval Research Laboratory (NRL) [39], and while tested additionally on RITS-6, produced experimental results that were judged to be less successful than those produced by the slow DC-heat method. We thus focus on the long-time DC heating method exclusively here.

It was previously mentioned in the description of the RITS experimental hardware (Section II) that the anode-side hardware penetrates the dustbin wall, so that supplementary hardware such as the in-situ DC heating system can be inserted through the dustbin wall. This eliminates any restriction on overall length of any DC heating design. A schematic view of the DC heating hardware that was developed and fielded is shown in Fig. 22. In this Figure, the cathode is indicated at the far left, and next to it (shaded darkly) is the Ta anode, shown in a ‘tabbed’ configuration rather than a solid circle, as is typical for the unheated configuration. The addition of the tabs, and the rather lengthy current feeds, is meant to minimize heat

transfer away from the anode, and to allow for gradients in temperature so that non-refractory materials such as aluminum could be used in the heating circuit. The circuit element delivering the heat to the anode is a disc of boron nitride (BN), shown just behind the tabbed Ta disc and to its right, and in physical contact with the Ta. BN was chosen because it is a refractory material, and thus can be expected to survive the relatively long time expected for any DC heating current to be delivered. Because the heating of the Ta is from contact with the BN, it can be expected that the surface temperature of the Ta surface facing the cathode, the relevant surface for these heating experiments, would be lower than the temperature of the backside facing the BN disc.

The heating protocol for the Ta anode, e.g. length of heating time, rate of temperature rise, and peak temperature achieved, is informed by the development of a temperature desorption curve for the Ta anode. To produce such a curve, the Ta anode was used as a circuit element in a heating system developed off-line in a light-laboratory environment. Heat was applied to the circuit in a vacuum chamber, increasing at a fixed rate ($1^{\circ}\text{C}/\text{sec}$ was typically used), and gasses evolving off the Ta were analyzed by a residual gas analyzer (RGA). Data available in the literature [40] regarding desorption from Ta indicate that the easiest-to-desorb substances are water vapor (H_2O) and hydrogen (H_2). More tightly bound oxides such as CO and gases such as O_2 and N_2 , require heating temperatures considerably beyond those required for H_2O and H_2 [41].

Data from light-laboratory DC heating experiments conducted at Sandia are presented in Fig. 23. The heating rate used resulted in an increase of $1^{\circ}\text{C}/\text{sec}$. It can be seen that as the Ta temperature is raised, desorption of H_2O begins at approximately 200°C , and is complete by 400°C . That is, as the temperature is raised beyond 400°C , very little if any H_2O is measured by the Residual Gas Analyzer (RGA) monitoring the desorption. For H_2 , desorption begins at $\sim 300^{\circ}\text{C}$, and rapidly increases to its peak at just over 600°C . The desorption rate then falls so that by an attained temperature of 1000°C , the vast bulk of the H_2 can be considered removed from the Ta. In the case of CO, significant desorption does not begin until a temperature greater than 900°C , with peak desorption occurring at well beyond 1000°C . Peak desorption rates for O_2 and N_2 occur at even higher temperatures.

Given the presence of a considerable amount of aluminum diode components in the diode region, any practical DC heating scheme must limit the maximum heating excursion near the diode. The desorption data clearly indicate that for an attained Ta surface temperature of $\sim 1000^{\circ}\text{C}$, almost all the H_2O and H_2 should be driven out of the Ta. This still leaves the heavier gasses and tightly bound oxides still present in the Ta. However, the hydrogen component is expected to be the largest quantity of the gases that could

desorb during the SMP power pulse, so that a peak Ta surface temperature of $\sim 1000^{\circ}\text{C}$ could be expected to be very effective at contaminant gas removal.

The resulting heating protocol chosen for the BN heating element was to raise the heating temperature over the course of approximately 20 minutes to a temperature of 800°C until 5 – 10 minutes before RITS was fired (resulting in $\sim 600^{\circ}\text{C}$ on the Ta anode surface). At that time, the heating element was ramped to 1200°C (850°C on the anode surface). The heater was then disconnected just before RITS was fired. For heated Al-coated anodes (and anodes with free-standing foils), the heater was set so that the anode surface was $\sim 630^{\circ}\text{C}$ for at least 30 minutes before shot time. For shots in which free-standing Al foils were heated, the heater was set so that the foil temperature was $\sim 400^{\circ}\text{C}$ at shot time. These temperature profiles were informed from the light-laboratory desorption measurements already discussed.

As already mentioned previously [14], measurements of copper samples activated by counter-streaming ions entering the cathode structure during the ensuing power pulse show conclusively show that all hydrogen was removed from the counter-streaming ions. Since hydrogen can be considered the most loosely bound of possible contaminant gases, point 1) listed above can be considered confirmed in these RITS experiments. It may be asked as to whether removal of all such ions in the A-K gap is the preferred outcome, since it is the presence of ions on the anode-side of the A-K gap that causes the final small-diameter pinch-in, as discussed earlier. It is pointed out that ions are still present in the A-K gap, such as from the tantalum ions comprising the anode material, and from oxides not removed by the relatively low-level DC heating used here. Secondly, the anecdotal presence of premature impedance collapse is still attributed, at least in part, to the presence of excess ions evolving in the A-K gap from contaminant ions, so that removal of the hydrogen component is regarded as a positive development.

The surface appearance of the Ta is observed to change considerably after the DC heating cycle. Before- and after-heating images of the Ta surface are shown in Figs. 24a and 24b, respectively. The dark-looking Ta surface in Fig. 24a (typical of as-provided Ta) is transformed into a clean and shiny-looking surface in Fig. 24b. In addition, the clean surface appearance after heating is not temporary, but persists for extended periods of time. Anecdotally, there are samples of the NRL pulse-heated Ta that continue to show a clean appearance for months or even years, without being stored in a dry-box [42].

V2. RF discharge cleaning. In this process, the diode region is evacuated, and a ~ 800 mT plasma source is introduced, with the discharge composed of molecules, atoms, and ions. The process gas is composed

of a 80% argon-20% oxygen mixture. The argon plasma kinetically cleans and physically sputters adsorbed contaminants from surfaces in the diode region, reducing the number of monolayers present on the surfaces. The oxygen reacts with carbon-based molecules, forming CO and CO₂. This energetic process produces a ‘glow’ on the affected metal parts. This glow can be seen in the photographic image in Figure 25. In the image, the A-K gap can be seen on the left side. In the RITS cleaning protocol, the RF discharge is struck and allowed to run for approximately 30 minutes. It is certainly clear that RF cleaning can remove contaminants from the A-K gap region. A side-effect of the glow discharge is that an unknown amount of contaminants can be liberated from surfaces outside the immediate A-K gap region, such as side-walls of the vacuum chamber located some distance away. Those contaminants may be pumped away in the general exhaust stream, or they might be re-deposited near the A-K gap, thus compromising the effect of the direct contaminant removal.

RF discharge cleaning as implemented on the RITS SIMP diode results in a very complex outcome, some aspects of which are not well understood. A more thorough discussion is planned for the upcoming separate publication mentioned above. A relative handful of SMP shots were taken in which RF cleaning was used, both in combination with DC heating, and by itself. The tentative conclusion from data analysis is that the RF cleaning by itself may have improved diode performance incrementally, but the effect of DC cleaning, either by itself or in conjunction with RF cleaning, is judged to be more significant. In the discussion below, featuring results from both heated and cleaned 12.5 – 12 and 8.5 – 8.3 shots, the particular configuration used will be stated. For the most important results, that of heated/cleaned 8.5 – 8.3 shots, both systems were used, and given the small amount of successful shots to be discussed, the effect on the final performance of either system by itself cannot be determined. A more definitive conclusion about the relative merits of either system, working solely or together, would be the subject of future experiments. In view of the apparent successful outcome of successful heating/cleaning of the smaller 8.5 – 8.3 SMP diode as fielded on RITS (detailed below), such future experiments would be highly recommended.

We note here that the additional hardware associated with the heating/cleaning capability presented additional material in the attenuation path of radiation measured by the axial PIN_0 monitor. Estimates of the amount of additional attenuation were made using ITS-CYLTRAN techniques [23]. The result is that the PIN_0 signal on a DC-heated shot must be multiplied by factor 1.21 in order to be compared to a PIN_0 signal on a non-heated shot.

V3. DC heating of the 12.5 -12 configuration. As stated previously, this configuration (operated at 7 – 8 MV output) resulted in the most stable performance of any configuration tested at any output voltage on RITS. Radiation pulse FWHMs were consistently measured, with few exceptions, to be full-pulse (> 45 ns), with any number of modifications to the standard Al-foil over Ta anode. These include removal of the Al-foil (bare Ta surface), replacing the free-standing Al foil with a ~ 1 μm-thick sputter-deposited Al coating, and substitution of other elements for Al in sputtered coatings. In some of these alternate-coatings cases, the resultant radiation pulse FWHM was observed to be reduced by premature impedance collapse, but the number of experiments was relatively small, so the cause of the reduced FWHM was difficult to discern. One coating for which consistent FWHM reduction occurred (for both the 12.5 – 12 and 8.5 – 8.3 configurations) was when gold replaced the standard aluminum material. This seems anecdotally to be a puzzling result, assuming again that the predominant cause of shortened pulse FWHM is increased contaminant inventory in the A-K gap. Gold is known to be a particularly clean metallic element. No determination was made in the RITS experiments for the cause of reduced FWHM associated with the use of gold coatings.

Given that the 12.5 – 12 configuration demonstrated stable performance for the most part at the 7 – 8 MV level on RITS SMP shots, the addition of DC heating to this configuration was not expected to lead to substantive improvements to diode performance, but instead experiments were undertaken to benchmark the performance of the heating/cleaning hardware compared to the ‘standard’ non-heated hardware. In that regard we note that the performance of the 12.5 – 12 configuration with heating/cleaning hardware in place, but not being used, *actually deteriorated compared to ‘standard’ non-heated shots*, i.e. shots in which no additional heating/cleaning hardware was in place. Radiation output and FWHM, even with the 1.21 factor included, were less than with a standard Al-foil shot. Consequently, any discussions about comparisons between ‘unheated’ and ‘heated’ shots should make clear what the ‘unheated’ configuration used in the comparison is, whether that is with ‘standard’ unheated shots, or with shots with heating/cleaning hardware installed but not operational. For all discussions below comparing heated/unheated shots, the unheated configuration is the standard one with the Al-foil in place.

The 12.5 – 12 heating experiments did not produce improvements to diode performance, as expected. But the experiments did yield one notable experimental result. Given that the hydrogen component of the counter-streaming ion current is shown conclusively to be removed, one might then expect the overall diode impedance to increase due to heating. Neither the 12.5-12 nor the 8.5-8.3 configurations behaved in this manner. The diode impedance in the 12.5-12 configuration actually *decreased*, and in the 8.5-8.3

configuration, the diode impedance remained the same. These results are addressed in the context of the SMP diode viewed as part of the IVA-SMP system in the second of these two papers.

V4. DC heating of the 8.5 – 8.3 configuration. When comparing the radiation FWHM values between the 12.5-12 and 8.5-8.3 configurations, it should be pointed out that ‘full-pulse’ FWHM for the 8.5 – 8.3 configuration is shorter than for the 12.5 – 12 configuration, by $\sim < 5$ ns. This is because the earlier-rising and added current in the lower-impedance 8.5 – 8.3 configuration contributes a larger dI/dt inductive term which depresses the corrected voltage early in the pulse, leading to reduced pulsewidth compared to 12.5 – 12.

To investigate the effect of heating/cleaning the 8.5 – 8.3 configuration, we compare one of the shots in which heating/cleaning was judged the most successful, Shot 2067, and two other ‘standard’ 8.5 – 8.3 shots (i.e. unheated free-standing foil over Ta), 1772 and 1774. (Shot 1774 has already been discussed.) Shot 2067 was taken with bare Ta as the anode material (no Al), and with both DC heating and RF cleaning in operation. A plot showing both the I_A and I_L waveforms for the three shots is shown in Fig. 27. The waveforms for the two ‘standard’ shots show the signs of premature impedance collapse, on both the I_A and I_L signals. That is, the waveforms exhibit the second inflection point where they undergo abrupt increases in slope. Prior to this, however, it is evident that in the case of the load current I_L , there is almost no difference in magnitude between the unheated shots and the heated/cleaned Shot 2067. This behavior repeats that seen in Fig. 18, where two 4.5 MV shots are shown with and without premature impedance collapse. That is, prior to the collapse, the waveforms look the same. For these three shots, heating the diode region did not change the current flowing through the diode. Prior to the impedance collapse, the I_A current also did not change. What did change, however, is the radiation pulse FWHM. This is illustrated in Fig. 27, which shows the axial PIN_0 signals for the three shots. In the plot, the 2067 PIN_4 waveform has been scaled upward by factor 1.21, to reflect the attenuation represented by the presence of the extra heating hardware, as stated above. The FWHM of the 2067 PIN_0, at 42 ns, can be considered full-pulse for the 8.5 – 8.3 configuration. The 42 ns FWHM can be compared to the greatly reduced FWHMs of Shots 1772 and 1774 (19 and 21 ns, respectively). In this regard, and assuming that the performance of Shot 2067 is not anomalous, the result of heating/cleaning the 8.5 – 8.3 configuration could be considered a success.

We will comment more on whether the 2067 performance should be considered typical later on in this discussion. While the FWHM for Shot 2067 increased greatly compared to the standard unheated shots it is compared with, the reason does not appear to be due to either a decrease in diode current (caused by

say a reduction in A-K gap contaminants), nor to a change in the radiation environment in general. This can be seen by comparing the PIN₀ signals of Shots 2067 and 1772 (Fig. 27). Prior to the radiation collapse seen in the latter waveform, the two signals are observed to be almost identical on the rise. The load current I_L and the axial radiation signal on the two shots are the same, prior to the impedance collapse seen in Shot 1772. Thus, heating/cleaning seems to have had no measurable effect on observable diode parameters such as the I_A and I_L currents (prior to any impedance collapse on the ‘standard’ shots). The diode impedances (not shown here) of the three shots are observed to be identical prior to the impedance collapse observed in 1772 and 1774. Comparison of the spot size and current density waveforms of the three shots indicates that prior to the impedance collapse seen in Shot 1772 and 1774, the respective waveform behaviors are virtually identical. We are left with looking for other clues as to the difference in performance.

One significant difference in radiation performance between Shot 2067 and 1772/1774 can be seen in Fig. 28, which compares the normalized PIN₀, PIN₄₅, and PIN₉₅ waveforms for the heated Shot 2067. This figure should be compared to the same waveforms plotted for Shot 1774, already shown in Fig. 12. (The PIN signals for Shot 1772 look very similar to Fig. 12.) In the case of Shot 1774 (Fig. 12), the three PIN signals rise together, but separate near their respective peaks, with PIN₀ peaking earlier than PIN₄₅ and PIN₉₅. Then the latter PINs peak almost 8 ns later than PIN₀. This has the tell-tale signs of an instability in the pinch, as discussed previously in connection with Figs. 12 and 19a-c. By contrast, the PINs on Shot 2067 (Fig. 28) show a remarkable consistency, rising and falling together, and undergoing a mid-pulse excursion together, with no temporal separations in local peaks. This is highly unusual behavior, seen in only a handful of shots, all of them taken with the heated 8.5 – 8.3 configuration.

One interpretation of the 3-PIN signature behavior on Shot 2067 is that the pinch-angle of the electron beam does not change during the power pulse. This would occur even as the magnitude of the dose-rate changes. If such a stable pinch-angle behavior could be validated, and if such a stable behavior could be shown to extend the radiation FWHM, then this would be a significant result that would be attributable to DC heating/cleaning. As a further measure of the successful performance of Shot 2067, we compare the spot size and current density (measured from TRSD) from 2067 with one of the most successful standard 12.5 – 12 shots, Shot 1908. This shot was already discussed in Section III, and results compared with Shot 1774 (8.5 – 8.3) in Figs. 9-11. The two spot sizes and current densities are compared in Figs. 29a and 29b, respectively. In Fig. 29a, the 2067 spot size, initially smaller than 1908, continues to fall even as the 12.5 – 12 spot size increases, a feature seen on many if not most 12.5 – 12 shots. Even with the later-

time jump in the 2067 spot size, it continues to run smaller than 1908. As for current density, while on Shot 1908, this peaks at 4.5 MA/cm^2 then falls, again similarly with many 12.5 -12 shots, on Shot 2067, the current density continues to rise until it reaches 8.2 MA/cm^2 . Even after the steep fall in 2067 current density later in the pulse, the level is still above the 1908 equivalent. Thus, the goal of heating the 8.5 – 8.3 configuration, e.g. to retain the smaller spot size of the 8.5 – 8.3 diode while extending the radiation FWHM, appears to have been realized.

The key question which remains is: can the performance seen in Shot 2067 be expected to become typical of heated/cleaned 8.5 – 8.3 shots? This is a difficult question to answer, given the relatively few examples of the configuration that have been tested. The use of heated bare Ta anodes occurred at the end of the allotted time given to tests of heating/cleaning, and further experiments are not likely in the near future. One other shot performed nearly as well as 2067 (Shot 2065), but featured compromised forward-going generator power. Insufficient numbers of shots thus occurred for the success of Shot 2067 to be considered statistically significant. If the Shot 2067 configuration performance produced a diagnostic signature clearly distinguished from non-heated standard 8.5 – 8.3 shots, then those variations in signature could be further investigated, even without additional shots being taken. But as we have seen, the primary difference pointed out here is the uniform-shape waveforms of the various PIN monitors compared to those in the standard shots. But the impedance, estimated diode voltage, and pinch dynamics (current density, spot size) of the heated/cleaned configuration do not vary significantly between the heated/cleaned and standard 8.5 – 8.3 shots.

With these observations in mind, any conclusions reached here concerning the success of the heating/cleaning protocol for the 8.5 – 8.3 shots must be considered provisional only, given the relatively small number of data points. Still, there is encouraging evidence that heating/cleaning (and again, these cannot be separated here) can act to extend the FWHM of the 8.5 – 8.3 configuration, which was in fact its purpose. If a more extensive experimental set could confirm this, then the possibility exists that the heating/cleaning protocol, combined with either hard collimation or limited target (to be described later in this paper), could yield a successful radiography platform.

VI. SUMMARY AND CONCLUSIONS

The goal of an electron beam-driven radiographic diode is the production of a high-current, high-voltage beam which is focused to as minimal a spot size as possible. Of the potential diodes which have been investigated for radiographic applications, the SMP diode is designed as a high-current diode, operated without an imbedded magnetic field. Compared to higher-impedance diodes, the SMP diode operates at

an impedance (~ 60 ohms or lower) which is a good match for a low flow-impedance MITL such as provided by RITS-6. However, there are several elements of SMP operation that complicate the control of diode dynamics necessary to achieve optimum spot size: 1) The counter-streaming ion population in the ‘standard’ SMP diode, which is required to pinch the electron beam to a tight focus, consists of contaminant ions which originate either from adsorbed surface monolayers, or from interstitials from the Al foil or tantalum interior. In-situ heating may prove to be one approach to adequately control the ion population. But even with in-situ heating, the core of intense beam operation is the generation of high-density electrode plasmas that can act to load down or even terminate the diode pulse. 2) The intense electron beam itself, operating without a guide field, contributes a potentially unstable configuration which in other experimental configurations has led to growth of such beam instabilities as resistive-wall or ion-hose. To date, no simulations of SMP diode behavior have indicated that such instabilities exist. But their presence is indicated in the wealth of anecdotal data presented in this paper. And 3) perhaps most importantly, the coupling of an SMP diode to an IVA leads to the dilemma of what to do with the incoming electron flow current, which is generally thought to be of sufficiently uncontrollable behavior that diversion of this current away from the diode region is considered the safest approach to SMP operation. As will be seen more clearly in the second of these two papers, this diversion appears, at least in the RITS geometry, to be of only temporary duration, and the resulting return of the flow to the diode region can lead to possibly unwanted effects for SMP diode dynamics.

Each of these potential complications to SMP operation has been systematically addressed in this paper. Key analytical tools were developed: 1) quantification of estimated diode voltage (V_{CORR}), calculated from MITL voltages upstream of the diode, and inductively corrected using the presumed diode current IBEAM. While inductive correction is not a new technique, one advance over previous work is to locate the point of MITL voltage closer to the diode, by demonstrating that V_{CORR} calculated using the G position (V_{CORR_G}) yields a viable estimate of the load voltage. The derived V_{CORR_G} is also self-consistently related by IV^x scaling to the three PIN diodes located at various angles to the radiation axis [23]; and 2) by quantifying the ‘Radiographer’s Equation’ in the axial direction (Table 1), and relating this scaling to the off-axis dose-rates (PIN_45 and PIN_95), an advance is made beyond the static x-factor in IV^x scaling use by previous researchers to an estimate of the evolution of the x-factor with time. The x-factor is of course related to the angle(s) at which the incoming pinch electrons impinge on the Ta converter. A changing x-factor implies that the electron pinch angle evolves over time. This fielding technique has application not only SMP diodes, but for any type of load that generates an electron beam.

The characterization of the changing electron angle on the converter with time, particularly with shots with truncated FWHMs, led to several key inferences: 1) For A-K gaps less than the ‘optimal’ 1:1 aspect ratio, the explanation of early-peaking axial dose-rate is shown to be caused primarily by the steepening over time of the electron angle to the converter, and not a decline in diode voltage (although this can contribute); and 2) comparison of the three PINs at various angles leads to the hypothesis that on many if not most shots with truncated radiation FWHMs, a developing perturbation of the electron beam angle suggestive of some kind of instability terminates the radiation pulse, and not the convergence of electrode plasmas, as has been previously asserted. Since no simulations of SMP diode have to date shown the occurrence of such an instability during the SMP power pulse, considerable space is devoted to developing a strong anecdotal case for the presence of some kind of inferred instability.

The possible presence of such instabilities plays an important role in one of the central hypotheses of this paper: that in-situ heating of the 8.5-8.3 SMP diode, the smaller of the two diodes investigated at the 7-8 MV output level, may be a way to extend the radiation pulse of the smaller cathode by stabilizing the electron beam pinch. This would take advantage of the indicated smaller spot size of the 8.5-8.3 configuration, compared to the larger (and more stable) 12.5-12 configuration. In order to develop this argument, the characterization of both 12.5-12 and 8.5-8.3 configurations is shown. Beyond the phenomenological description of spot size and its evolution, it is shown from cross-referencing the separate TRSD diagnostic, PIN signals, and current waveforms, that there may be a causal mechanism implied in the smaller spot size measured on 8.5-8.3 shots. That is, it is the tendency of the electron pinch to turn progressively inward that appears to maintain the smaller spot size over the 8.5-8.3 power pulse. By contrast, the more stable (and straighter) pinch apparent in the 12.5-12 shots appears to result in larger spot size. Self-consistent comparisons of such variables as IV^x scaling and diode impedance lead to a comprehensive picture of the scaling of dose with A-K gap seen in the 4.5 MV A-K gap scan series. Such an overview can replace the more limited and anecdotal observations of previous researchers, such as the tendency for SMP performance to peak near the 1:1 aspect ratio, or the tendency of spot size in 12.5-12 to peak early, then rise. The smaller 8.5 cathode size gives rise to current densities in the A-K gap of up to 8 MA/cm². It could simply be that current densities of such magnitude are more prone to instability growth.

While the in-situ heated results for the 8.5-8.3 diode are encouraging, the small dataset supporting the in-situ heating thesis precludes our conclusion that heating is a validated approach to increased FWHM for 8.5 mm cathodes (or perhaps any smaller configuration in a SMP dataset). More experimental work is needed to confirm this.

Use of alternate anode designs to decrease the beam spot size.

The implied emphasis in all of the discussion to this point about decreasing spot size is that beam behavior itself should be controlled to a smaller spot. This may be termed *unapertured anode operation*, since the entire anode surface shown in Figs. 2 and 3 is accessible to the focusing electron beam. There are alternatives to an unapertured anode that can be considered for reduction of spot size. The first is termed *hard-aperturing* of the anode [36]. In this design, a series of stepped conical structures is placed behind the anode, made of dense material like tungsten. The cone radius increases steadily with distance behind the anode plane, thus mimicking a pinhole camera, with the entrance to the cone defining the maximum spot size. That is, any electrons striking the anode beyond the cone entrance would produce photons that are absorbed in the tungsten conical structure. The second alternative is a *limited target* [36]. In this case, the broad anode plane is replaced by a delimited hi-Z material design, like a narrow tubular structure of constant diameter for some distance behind the anode plane. The anode plane itself can be defined by a thin foil. In this case, bremsstrahlung photons are only produced when electrons strike the narrow tube front (and possibly a slight amount on the tube sides). The diameter of the tube front then defines the spot size.

In both these cases of such an *apertured* anode, the effect of spot size growth and spot wander have a much more significant effect on radiographic performance, possibly even approaching the 50% reduction in dose due to FWHM reduction. Photons emitted from a growing spot area beyond the hard-apertured entrance or the limited target location are simply lost and don't contribute to dose. And any spot wander that exceeds the width of the limited target, say, would result in dose output ceasing almost entirely. If, on the other hand, techniques could be developed that would address and mitigate all three issues, e.g. FWHM reduction due to premature impedance collapse, spot size growth, and spot wander, then this could allow for the use of either *apertured* anode design, and thus have the spot size be determined externally from the inherent SMP spot size. That is, such mitigation would improve the reproducibility of dose output. If the resultant SMP spot size is bigger than that defined by the hard-apertured or limited anode, the facility size and/or output voltage could be adjusted to produce the desired dose output. The net result of such a technical path is that the inherent spot size of the SMP pinch itself is but one of the desired outcomes of SMP design.

Regarding the performance of the heated/RF cleaned 8.5 – 8.3 shots, if subsequent experiments can validate the smaller spot size and larger FWHM for a statistically significant number of shots, and if it can

be shown that spot wander can be also controlled, then this diode could be a candidate for an apertured anode configuration.

ACKNOWLEDGEMENTS

The authors acknowledge the technical support of the RITS-6 facility staff – Dan Nielsen, Derek Ziska, Bill Bui, Steve Cordova, Robert Obregon, Frank Wilkins, and Ray Gignac. Darryl Droemer provided key diagnostic support. The authors also gratefully acknowledge the key role of Dr. Bruce Weber of the Naval Research Laboratory in the execution of the ITS-CYLTRAN simulations required to quantify the ‘Radiographer’s Equation’ specific to the RITS geometry, and listed as Equation 4 in the text. The authors also acknowledge fruitful conversations with Dr. George Laity, also with Sandia National Laboratories. Derek C. Lamppa of Sandia assisted in the RF discharge cleaning experiments. Sandia National Laboratories is a multimission laboratory managed and operated by National Technology and Engineering Solutions of Sandia, LLC, a wholly owned subsidiary of Honeywell International, Inc., for the U.S. Department of Energy’s National Nuclear Security Administration under contract DE-NA0003525. The views expressed in the article do not necessarily represent the views of the U.S. Department of Energy or the United States Government.

Data Availability Statement

The data that support the findings of this study are available from the corresponding author upon reasonable request.

REFERENCES

1. G. S. Cunningham and C. Morris, *The Development of Flash Radiography*, Los Alamos Science, Number 28 (2003).
2. Consult the excellent review article: J. Maenchen, G. Cooperstein, J. O'Malley, and I. Smith, *Advances in Pulsed Power-Driven Radiography*, Proc. IEEE 92, 1021 (2004): and references listed therein.
3. M. S. Di Capua and D. G. Pellinen, *Propagation of power pulses in magnetically insulated vacuum transmission lines*, J. Appl. Phys **50** (1979) 3713 – 3720.
4. J. C. Martin, *J. C. Martin on Pulsed Power*, T. H. Martin, A. H. Guenther, and M. Kristiansen, Eds. New York: Plenum, 1996.
5. B. Etchessahar, B. Birel, B. Cassany, T. Desanlis, L. Voisin, R. Maissonny, M. Toury, L. Hourdin, F. Cartier, S. Cartier, T. D'Almeida, C. Delbos, A. Garrigues, D. Plouhinec, S. Ritter, D. Sol, F. Zucchini, M. Caron, *Experimental study of self magnetic pinch diode as flash radiography source at 4 megavolt*, Phys. Plasmas **20** (2013) 103117-1 – 7.
6. D. Hinshelwood, G. Cooperstein, D. Mosher, D. Ponce, S. Strasburg, S. Swanekamp, S. Stephanakis, B. Weber, F. Young, A. Critchley, I. Crotch, and J. Threadgold, *Characterization of a Self-Magnetic –Pinched Diode*, IEEE Trans. Plasma Sci. **33**, 696 (2005).
7. K.D. Hahn, N. Bruner, M.D. Johnston, B.V. Oliver, T. J. Webb, D.R. Welch, S.R. Cordova, I. Crotch, R.E. Gignac, J.J. Leckbee, I. Molina, S. Portillo, J.R. Threadgold, D. Ziska, *Overview of Self-Magnetically Pinched-Diode Investigations on RITS-6*, IEEE Trans. Plasma Sci. **38**, 2652 (2010).
8. N. Bruner, T. Genoni, E. Madrid, D. Rose, D. Welch, K. Hahn, J. Leckbee, S. Portillo, B. Oliver, V. Bailey, and D. Johnson, *Modeling particle emission and power flow in pulsed-power driven, nonuniform transmission lines*, Phys. Rev. Spec. Top. Accel. Beams **11** (2008) 040401-1 – 10.
9. S. A. Goldstein, R. C Davidson, J. G. Siambis, and R. Lee, *Focused-Flow Model of Relativistic Diodes*, Phys. Rev. Lett **33** (1974), 1471.
10. A. E. Blaugrund, G. Cooperstein, S. A. Goldstein, *Relativistic electron beam pinch formation processes in low impedance diodes*, Phys. Fluids **20** (1977) 1185–1194.
11. T.W.L. Sanford, J. A. Halbleib, J. W. Poukey, A. L. Pegenzer, R. C. Pate, C. E. Heath, R. Mock, G. A. Mastin, D. C. Ghiglia, T. J. Roemer, P. W. Spence, G. A. Proulx, *Measurement of electron-energy deposition necessary to form an anode plasma in Ta, Ti, and C for coaxial bremsstrahlung diodes*, J. Appl. Phys. **66**(1) (1989) 10-22.
12. LSP is a software product of ATK Mission Research, Albuquerque, NM.
13. Dale R. Welch, David V. Rose, Nichelle Bruner, Robert E. Clark, Bryan V. Oliver, Kelly D. Hahn, and Mark D. Johnston, *Hybrid simulation of electrode plasmas in high-power diodes*, Phys. Plasmas **16** (2009), 123102-1 - 9.

14. M. G. Mazarakis, N. Bennett, M. E. Cuneo, S. D. Fournier, M. D. Johnston, M. L. Kiefer, J. J. Leckbee, D. S. Nielsen, B. V. Oliver, M. E. Sceiford, S. C. Simpson, T. J. Renk, C. L. Ruiz, T. J. Webb, D. Ziska, D. W. Droemer, R. E. Gignac, R.J. Obregon, F. L. Wilkins, D. R. Welch, *Contribution of the backstreaming ions to the self-magnetic pinch (SMP) diode current*, Phys. Plasmas **25** (2018), 043508 -1 to 9.
15. D. Hinshelwood, R. Allen, R. Commisso, G. Cooperstein, B. Huhman, D. Mosher, D. Murphy, P.F. Ottinger, J. Schumer, S. Swanekamp, S. Stephanakis, B. Weber, F. Young, I. Crotch, J. O'Malley, and J. Threadgold, *High-Power Self-Pinch Diode Experiments for Radiographic Applications*, IEEE Trans. Plasma Sci. **35**, 565 (2007).
16. J. Threadgold, I. Crotch, D. V. Rose, J. Maenchen, *2-D LSP Simulations of the Self Magnetic Pinch Diode*, in 14th International Pulsed Power Conference (**PPC-2003**), Dallas TX, 2003, M. Giesselman and A. Neuber, Eds., ISBN 0-7803-7915-2, 995-998.
17. S. Swanekamp, G. Cooperstein, J. Schumer, D. Mosher, F. Young, P.F. Ottinger, and R. Commisso, *Evaluation of Self-Magnetically Pinched Diodes up to 10 MV as High-Resolution Flash X-Ray Sources*, IEEE Trans. Plasma Sci. **32**, 2004 (2004).
18. N. Bruner, D. Welch, K. D. Hahn, B. V. Oliver, *Anode plasma dynamics in the self-magnetic pinch diode*, Phys. Rev. Spec. Top. Accel. Beams **14** (2011) 024401-1 – 7.
19. N. Bruner, D. R. Welch, T. J. Webb, M. G. Mazarakis, M. L. Kiefer, M. D. Crain, D. W. Droemer, R. E. Gignac, M. D. Johnston, J. J. Leckbee, I. Molina, D. Nielsen, R. Obregon, T. Romero, S. Simpson, C. C. Smith, F. L. Wilkins, D. Ziska, *The impact of plasma dynamics on the self-magnetic-pinch diode impedance*, Phys. Plasmas **22** (2015) 033113-1 – 10.
20. N. Bennett, D. R. Welch, M. D. Johnston, and B.V. Oliver, 3-D simulations of the Self-Magnetic Field Diode, Voss Scientific VSL-1302 (unpublished).
21. Amitava Roy, R. Menon, S. Mitra, Senthil Kumar, Vishnu Sharma, K. V. Nagesh, K. C. Mittal, and D. P. Chakravarthy, Phys. Plasmas **16** 053103 (2009).
22. P. N. Martin, J. R. Threadgold, S. Vickers, *Critical Current Operation of the Optimized Self-Magnetic Pinch Radiographic Diode*, IEEE Trans. Plasma Sci. **41** (2013) 2510-2515.
23. T. J. Renk, B. V. Weber, I. M. Rittersdorf, and T. J. Webb, *Technique for inferring angle change as a function of time for high-current electron beams using a dose-rate monitor array*, Rev. Sci. Instrum. **90**, 114709 (2019).
24. N. Bruner, M. D. Crain, D. W. Droemer, R. E. Gignac, G. Lare, I. Molina, R. Obregon, C. C. Smith, F. L. Wilkins, D. R. Welch, S. Cordova, M. L. Gallegos, M. D. Johnston, M. L. Kiefer, J. J. Leckbee, M. G. Mazarakis, D. Nielsen, T. J. Renk, T. Romero, T. J. Webb, D. Ziska, *Shot Reproducibility of the self-magnetic-pinch diode at 4.5 MV*, Phys. Rev. Spec. Top. Accel. Beams **17** (2014) 050401-1 – 12.

25. Timothy J. Renk, Bryan V. Oliver, Mark L. Kiefer, Timothy J. Webb, Joshua J. Leckbee, Mark D. Johnston, Sean Simpson, and Michael G. Mazarakis, *Characterization of Self-Magnetic Pinch (SMP) radiographic diode performance on RITS-6 at Sandia National Laboratories: 1) Diode Dynamics, DC Heating to extend Radiation Pulse*, Sandia Report SAND-2021-13998, October 2021.
26. P. A. Miller and C. W. Mendel, *Analytic model of applied-B ion diode impedance behavior*, J. Appl. Phys. **61** (1987) 529-539.
27. P. F. Ottinger and J. W. Schumer, *Rescaling of equilibrium magnetically insulated flow theory based upon results from particle-in-cell simulations*, Phys. Plasmas **13** (2006) 063109-1 – 17.
28. P. F. Ottinger, T. J. Renk, and J. W. Schumer, *Method for improved voltage determination for pulsed power systems utilizing a magnetically insulated transmission line*, Phys. Plasmas **26**, 023105 (2019).
29. P. N. Martin, J. R Threadgold, A. Jones, J. McLean, G. M. Cooper, K. Webb, G. Jeffries, P. Juniper, *Investigations into the Role of the Bremsstrahlung Conversion Target in the Self-Magnetic Pinch Radiographic Diode*, IEEE Trans. Plasma Sci **39** (2011) 1943 – 48.
30. I. Crotch, *Radiographer's equations for megavolt electron beams*, IEEE Conference on Plasma Science (ICOPS 2004), p. 183.
31. HWH/JCM/82/8, *Re-evaluation of the bremsstrahlung production efficiency for optimum targets*, Atomic Weapons Research Establishment, England, Internal Memo.
32. T. H. Martin, *Determination of bremsstrahlung production efficiencies from data obtained on Phermex at 27 MeV*, Sandia National Laboratory Report SC-DR-69-240, May, 1969.
33. ----, *A computerized method of predicting electron beam bremsstrahlung radiation with specific application to high voltage flash x-ray machines*, Sandia National Laboratories Report SCRR-69-241, May, 1969.
34. D. E. Beutler, J. A. Halbleib, T. W. L. Sanford, and D. P. Knott, *Experimental Verification of Bremsstrahlung Production and Dosimetry Predictions as a Function of Energy and Angle*, IEEE Trans. Nulc. Sci 41, no. 6 (1994), 2727.
35. J. A Halbleib and T. A. Mehlhorn, *ITS: The integrated TIGER series of coupled electron/photon Monte Carlo transport codes*, Nucl. Sci Eng. **92 (2)** (1986), 338.
36. T. J. Webb, M. D. Johnston, J. J. Leckbee, B. V. Oliver, *Radiographic characterization experiments of the self-magnetic pinch diode on RITS-6*, Sandia National Laboratories SAND2012-10169, Albuquerque, NM, December 2012 (unpublished).
37. S. Portillo, S. S. Lutz, L. P. Mix, K. Hahn, D. Rovang, J. E. Maenchen, I. Molina, S. Cordova, D. Droemer, R. Chavez, and D. Ziska, *Time-Resolved Spot Size Measurements from Various Radiographic Diodes on the RITS-3 Accelerator*, IEEE Trans. Plas. Sci **34(5)** (2006), 1908-1913.
38. D. W. Droemer, M. D. Crain, G. A. Lare, N. Bennett, and M. D. Johnson, *An optical diagnostic for observing anode-cathode plasmas for radiographic source development*, 19th IEEE Pulsed Power Conference (PPC2013), San Francisco, CA, 2013, pp. 1-6. doi: 10.1109/PPC.2013.6627628.

39. Bruce Weber, Naval Research Laboratory, unpublished data.
40. F. Rosebury, *Handbook on Electron Tube and Vacuum Techniques*, Amer. Inst. Phys, New York, 1993.
41. Experimental data supporting this can be found in: B.V. Weber, R.J. Allen, B.G. Moosman, S.J. Stephanakis, F.C. Young, N.R. Pereira, J.R. Goyer, *Improved Bremsstrahlung from Diodes With Pulse-Heated Tantalum Anodes*, IEEE Trans. on Plasma Sci. **30 [5]** (2002), 1806-15.
42. Bruce Weber, private conversation.

TABLE CAPTIONS

Table 1. Coefficients and powers associated with Eq. 4. Listed for the three PIN directions, and for electron angles to the converter from 10 to 80 degrees, in 10-degree increments. Reproduced from [T. J. Renk, B. V. Weber, I. M. Rittersdorf, T. J. Webb, Rev. Sci Instrum. **90** (2019) 114709], with the permission of AIP Publishing.

FIGURE CAPTIONS

Fig. 1. Simplified conceptual diagram of radiographic interrogation.

Fig. 2. Schematic diagram of the RITS-6 downstream MITL and SMP load region.

Fig. 3. Closeup schematic view of the SMP diode and A-K gap.

Fig. 4. Schematic view of the RITS cell: top, includes converter package, PIN detector locations, and materials between the photon source and the PIN locations attenuating the photon flux. (Drawing not to scale). Reproduced from [T. J. Renk, B. V. Weber, I. M. Rittersdorf, T. J. Webb, Rev. Sci Instrum. **90** (2019) 114709], with the permission of AIP Publishing.

Fig. 5. Schematic depiction of TRSD fielding geometry.

Fig. 6. Typical image, fast streak camera. Time proceeds from bottom to top. Cathode and anode position along the x-axis. Radiation pulse occurs within the pink dashed lines.

Fig. 7. Load region current waveforms, Shot 1908, plus (scaled) PIN_0 dose-rate.

Fig. 8. Dose-rate monitors PIN_0, PIN_45, PIN_95, Shot 1908.

Fig. 9. Load region currents compared, Shots 1908 (12.5-12) and 1774 (8.5-8.3).

Fig. 10. Estimated load impedances, Shots 1908 and 1774.

Fig. 11. Spot size calculated from TRSD, Shots 1908 and 1774 (arbitrary units).

Fig. 12. Scaled dose-rates and IBEAM current, Shot 1774.

Fig. 13. 4.5 MV series, dose@1 meter as function of A-K gap.

Fig. 14. a. Peak dose-rates, PIN_0 (axial). b. Peak dose-rates, PIN_95 (95°)

Fig. 15. a. 'Successful' 7 mm shots: dose@ 1meter vs. A-K gap. b. Initial pinch angle vs. A-K gap.

Fig. 16. a. Z_{LOAD} vs A-K gap. b. PIN_0 vs A-K gap.

Fig. 17. a. I_L , Shots 1540 and 1558, and (scaled) Spot Size, 1558. b. PIN_0, Shots 1540 and 1558. c. Spot Size, Shots 1540 and 1558.

Fig. 18. I_L , Shots 1559 and 1536, and (scaled) PIN_0 signals, same shots.

Fig. 19. a. PIN_0, _45, _95, and interpolated electron angle (scaled), Shot 1774. b) Composite data plot, Shot 1774, with angle contours. c) interpolated electron angle and Spot Size (both scaled), Shot 1774.

Fig. 20. 4.5 MV series, radiation pulse FWHM as function of A-K gap.

Fig. 21. PIN_95 radiation pulse (double), Shot 1910.

Fig. 22. Schematic drawing of DC heating hardware.

Fig. 23. Measured desorption curves, heated Ta anode.

Fig. 24. a. Before and b. after-heating photographs of Ta surface.

Fig. 25. Photograph of diode region during RF discharge.

Fig. 26. I_L and I_A waveforms, Shots 2067, 1772, 1774.

Fig. 27. PIN_0, Shots 2067, 1772, 1774.

Fig. 28. PIN_0, _45, _95, Shot 2067.

Fig. 29. a. Spot Size, Shots 2067 and 1908. b. Current density, Shot 2067 and 1908.

Filters:	3.1 cm Al		5.85 cm Al		1 cm polycarb. + 1 cm Al	
e-angle	x_0	c_0	x_45	c_45	x_95	c_95
0	2.80	5037	2.48	1670	1.69	2878
10	2.68	4962	2.48	1686	1.71	2836
20	2.50	4537	2.51	1680	1.72	2893
30	2.36	4289	2.56	1664	1.74	2942
40	2.28	3900	2.57	1636	1.77	3030
50	2.21	3674	2.52	1578	1.81	3146
60	2.16	3562	2.44	1547	1.86	3223
70	2.14	3402	2.39	1515	1.93	3291
80	2.13	3307	2.36	1492	1.94	4339

TABLE 1

FIGURES

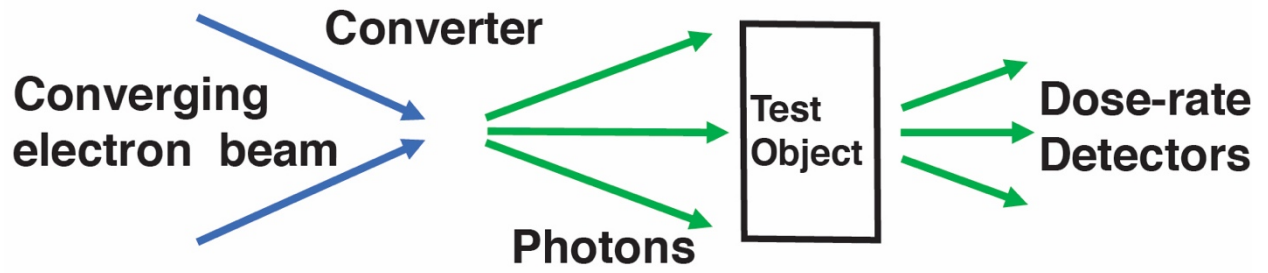


Fig. 1

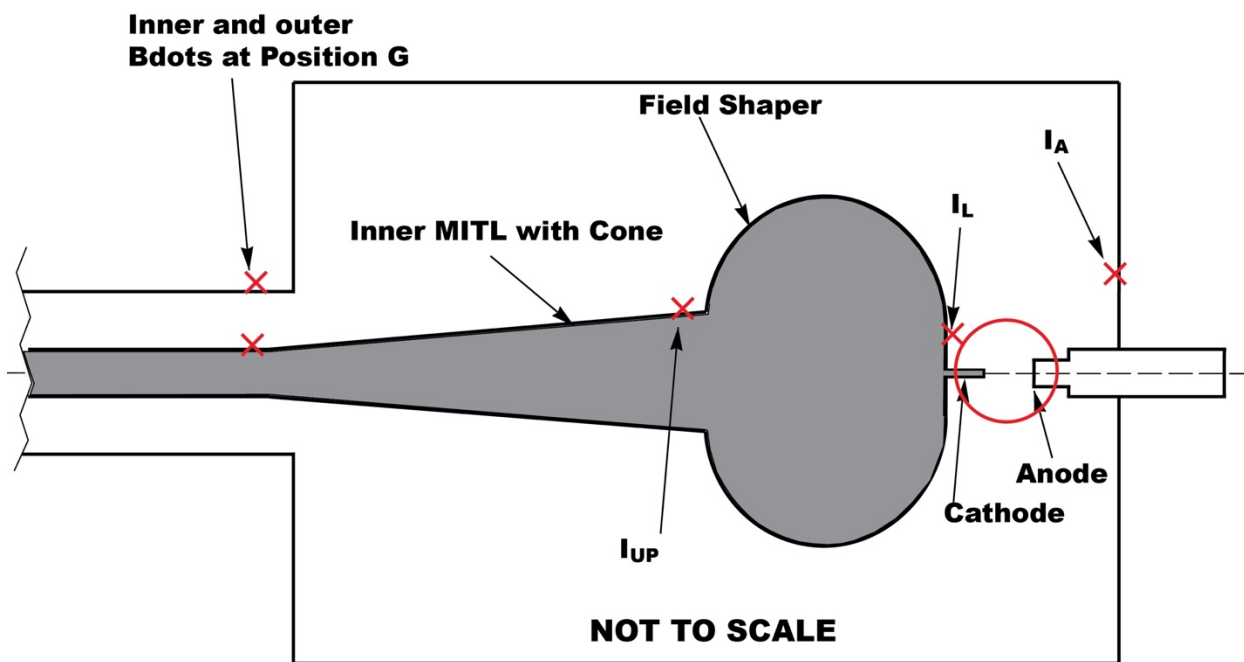


Fig. 2

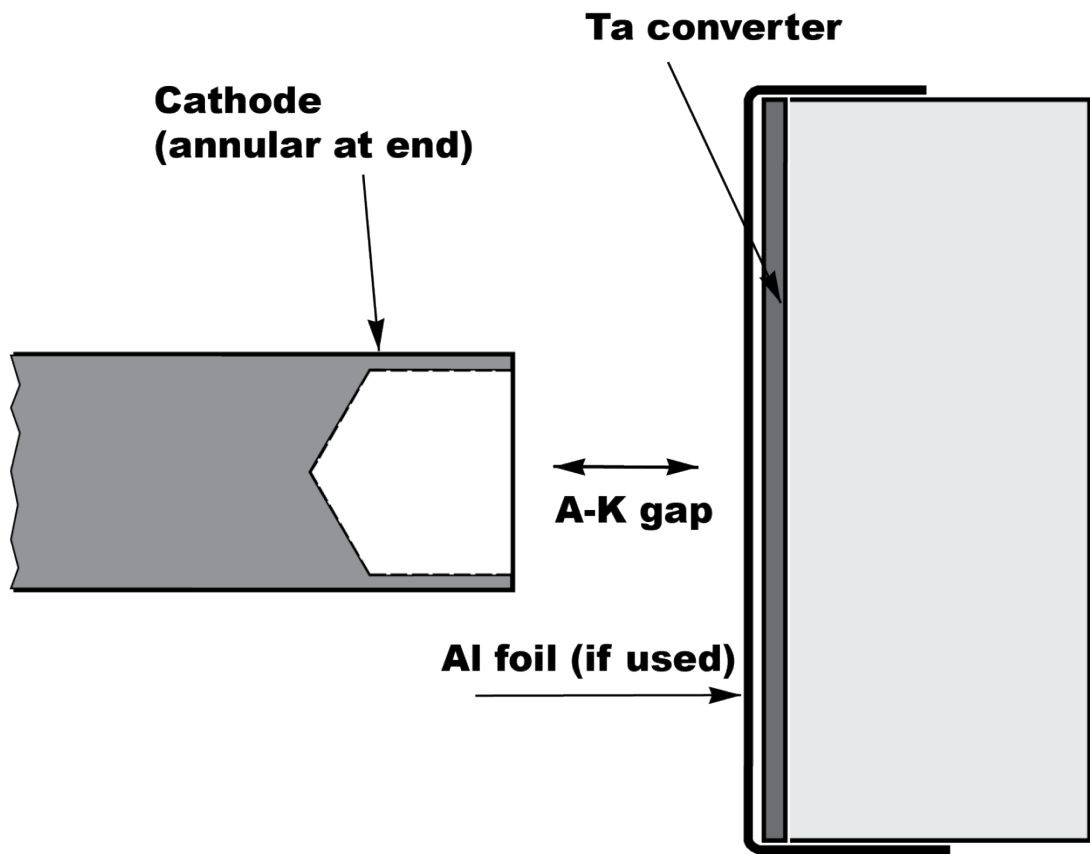


Fig. 3

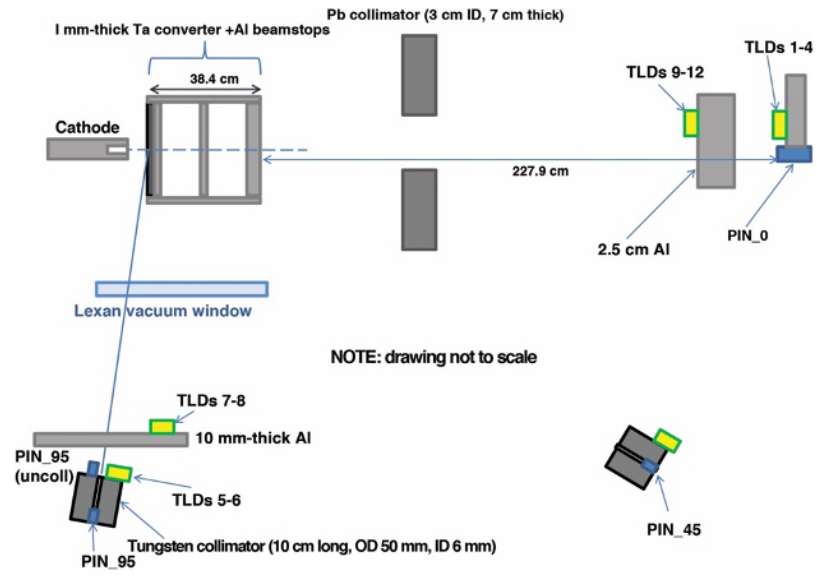


Fig. 4

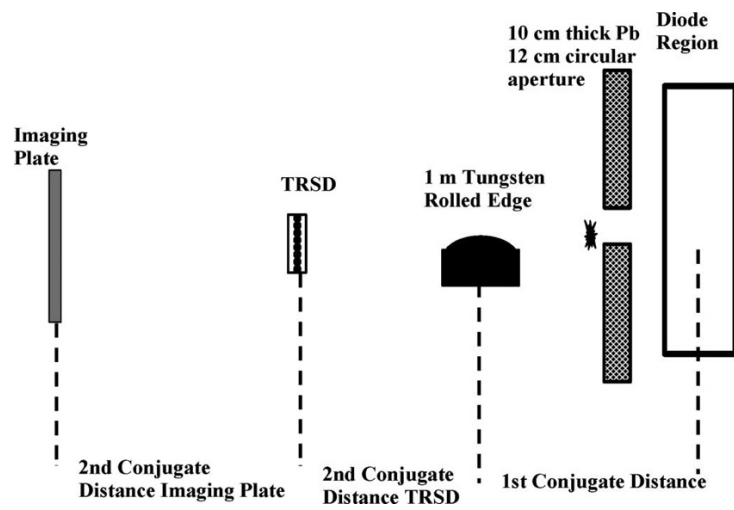


Fig. 5

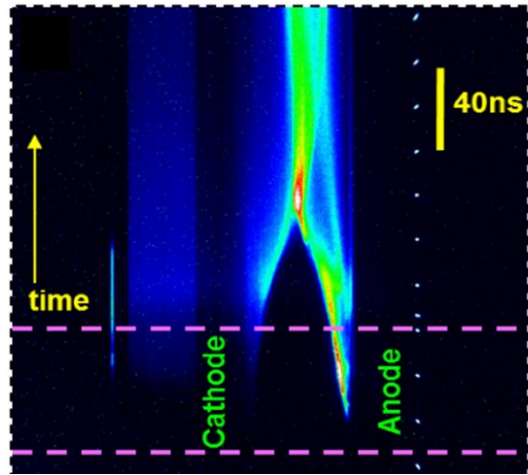


Fig. 6

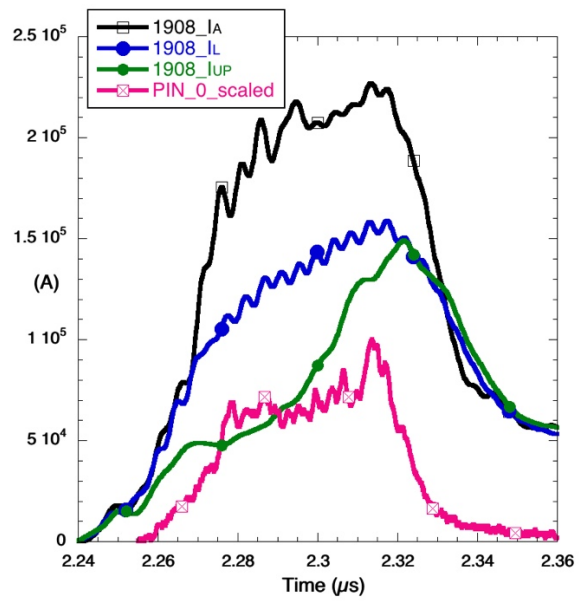


Fig. 7

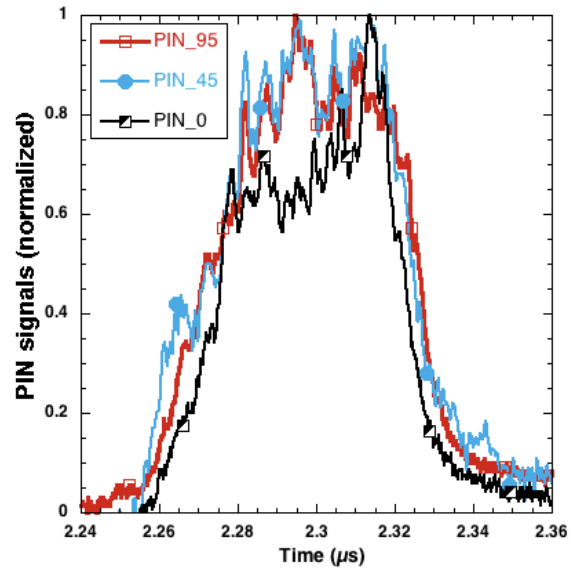


Fig. 8

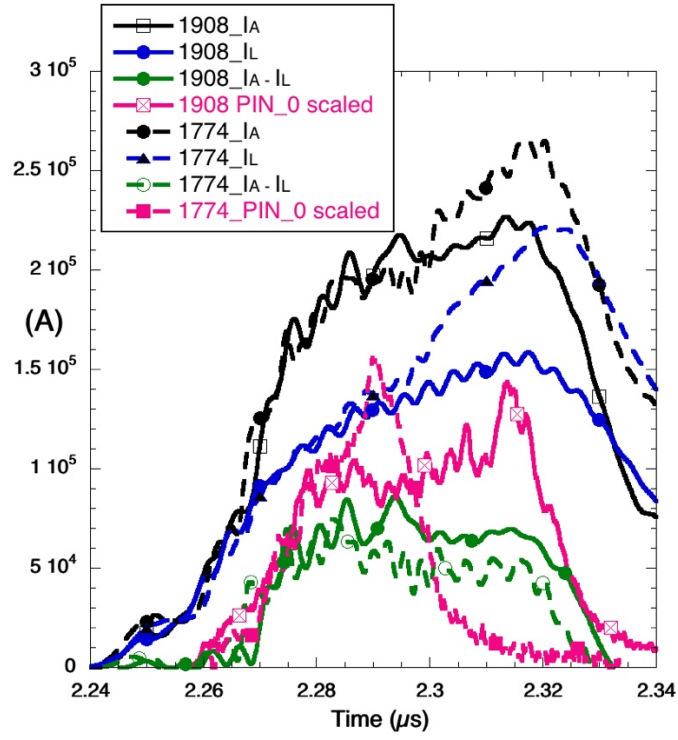


Fig. 9

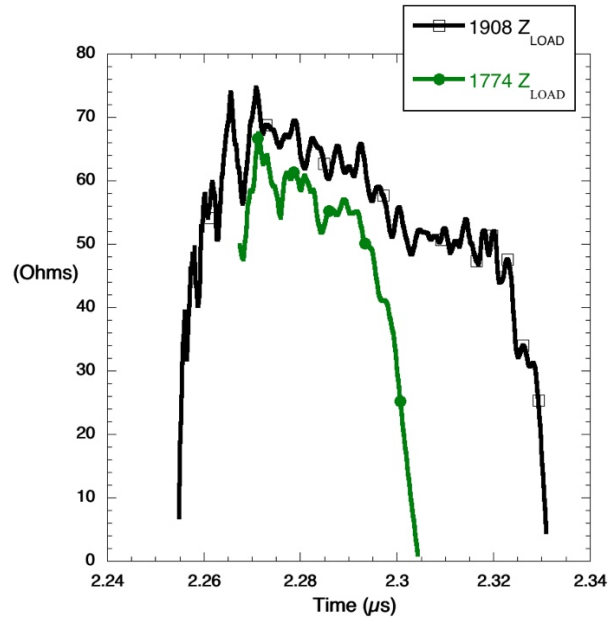


Fig. 10

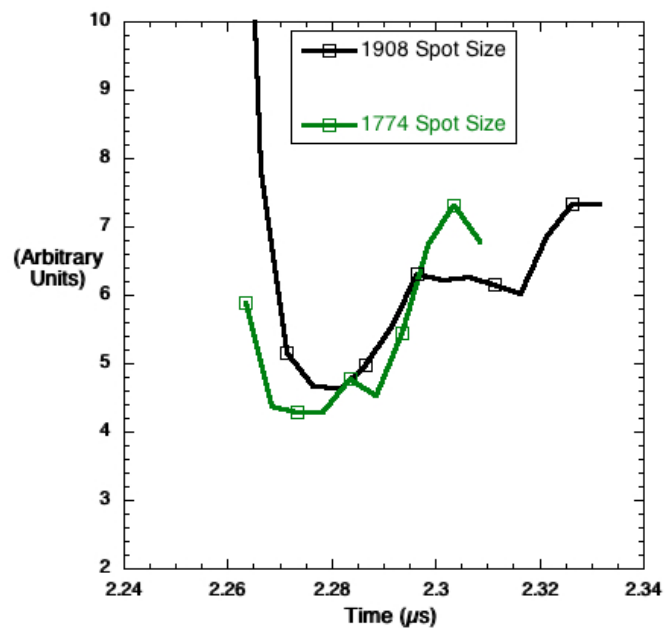


Fig. 11

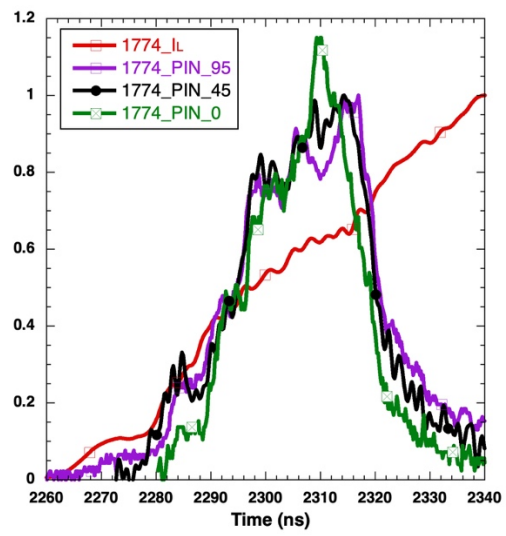


Fig. 12

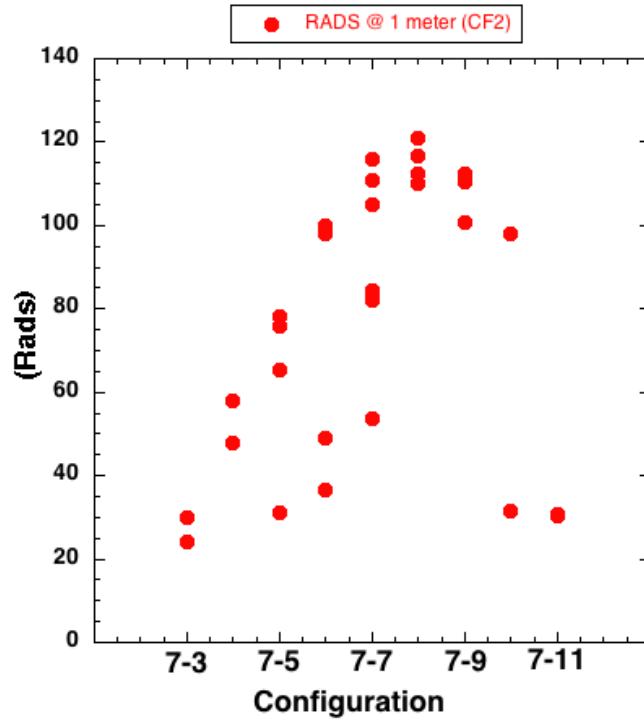


Fig. 13

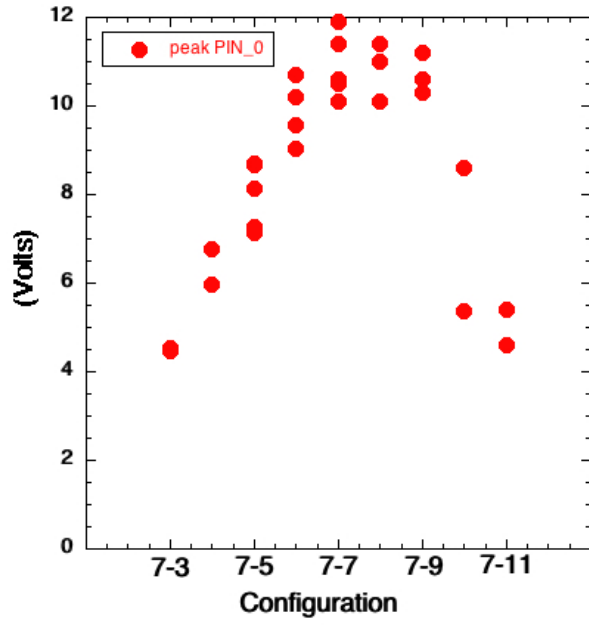


Fig. 14a

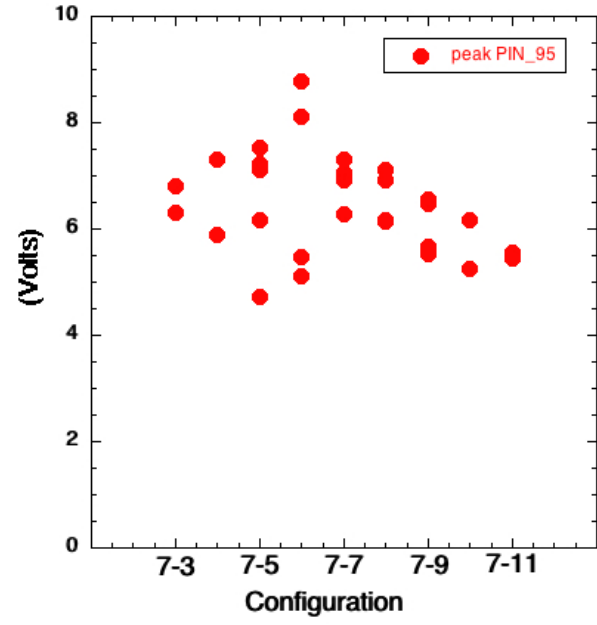


Fig. 14b

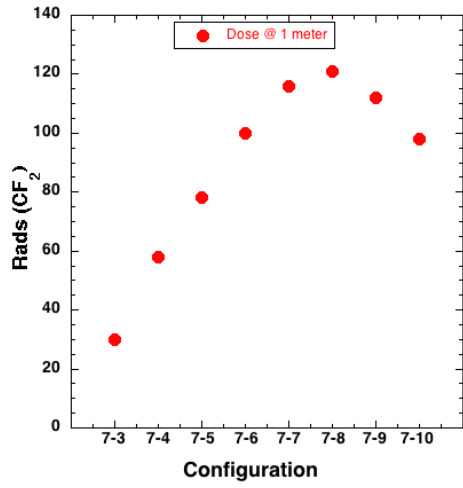


Fig. 15a

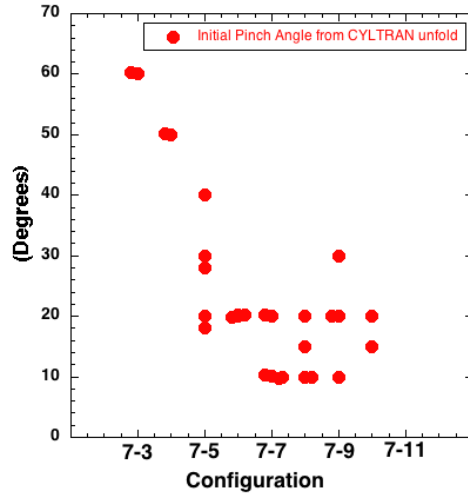


Fig. 15b

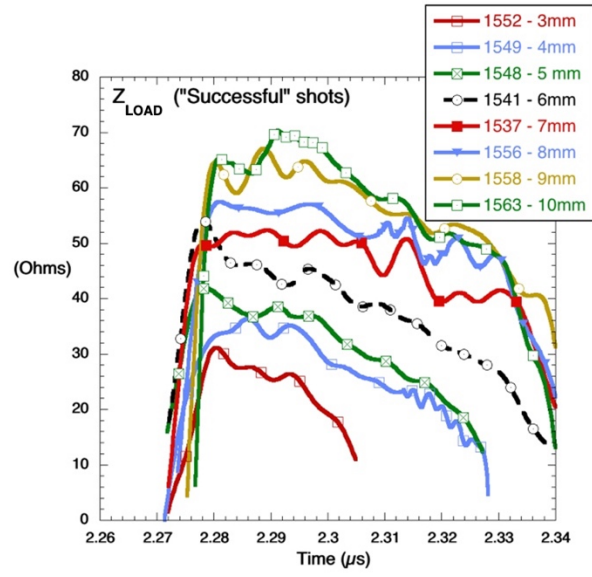


Fig. 16

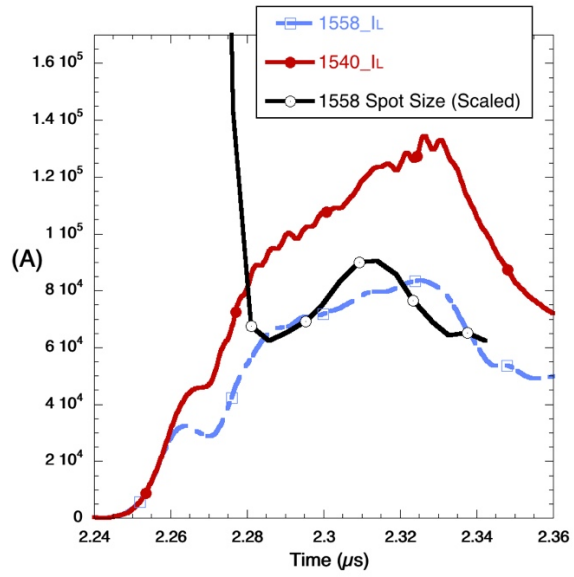


Fig. 17a

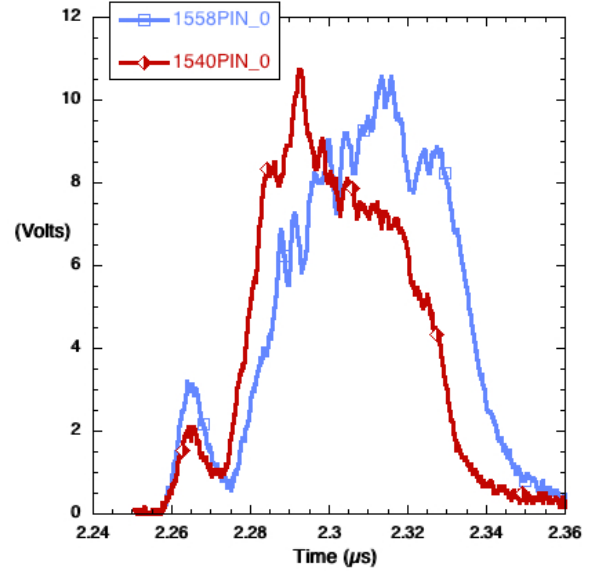


Fig. 17b

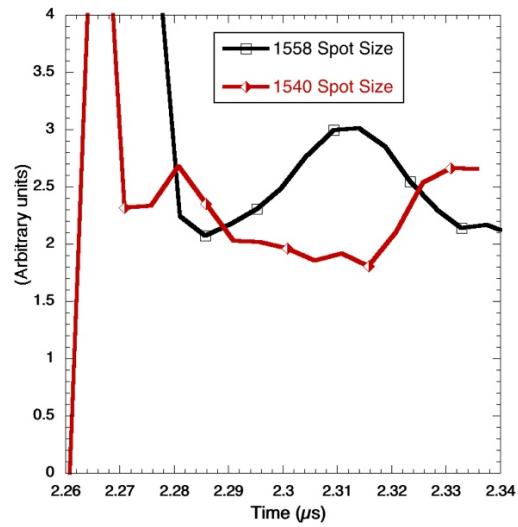


Fig. 17c

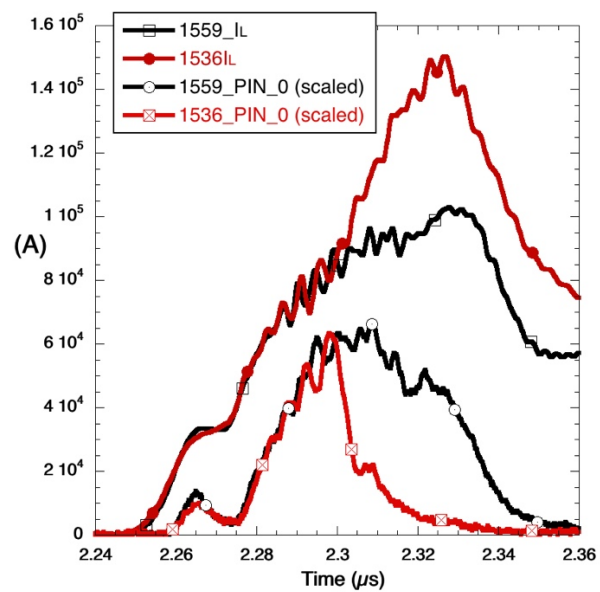


Fig. 18

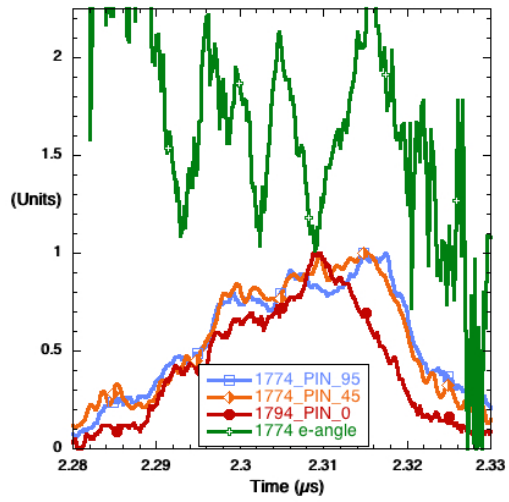


Fig. 19a

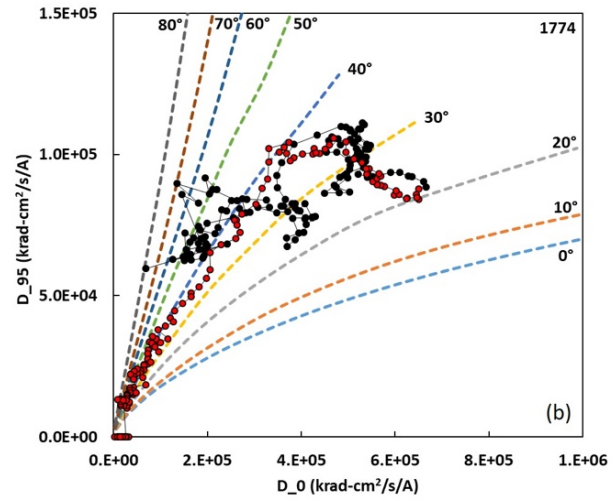


Fig. 19b

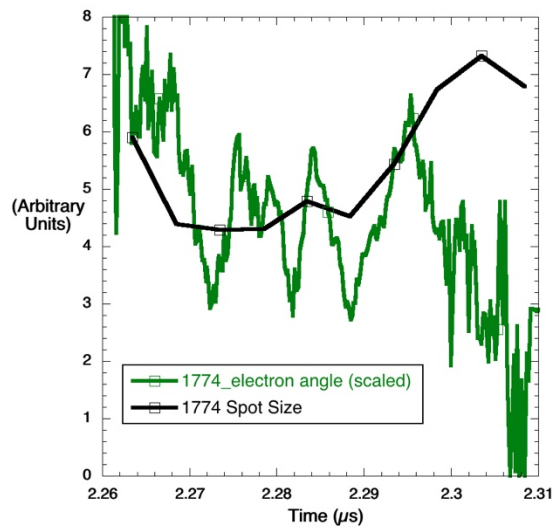


Fig. 19c

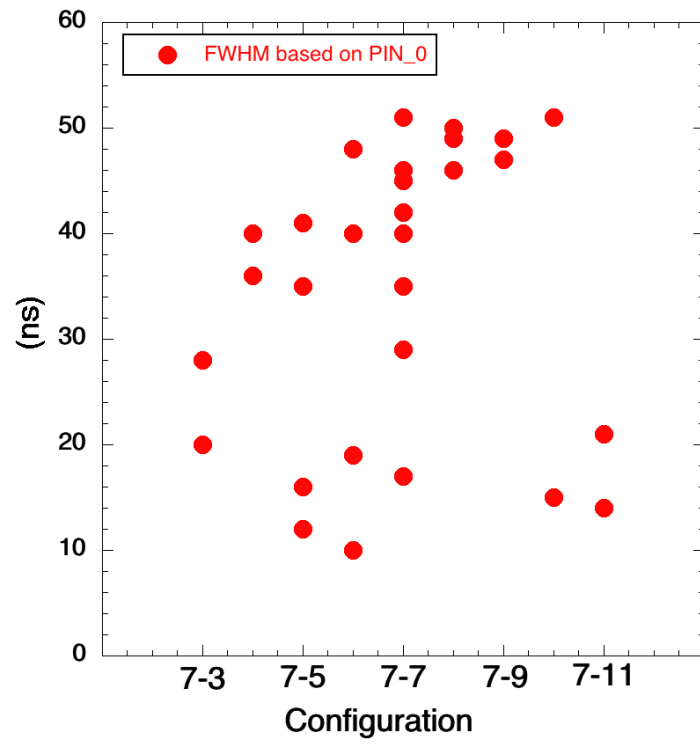


Fig. 20

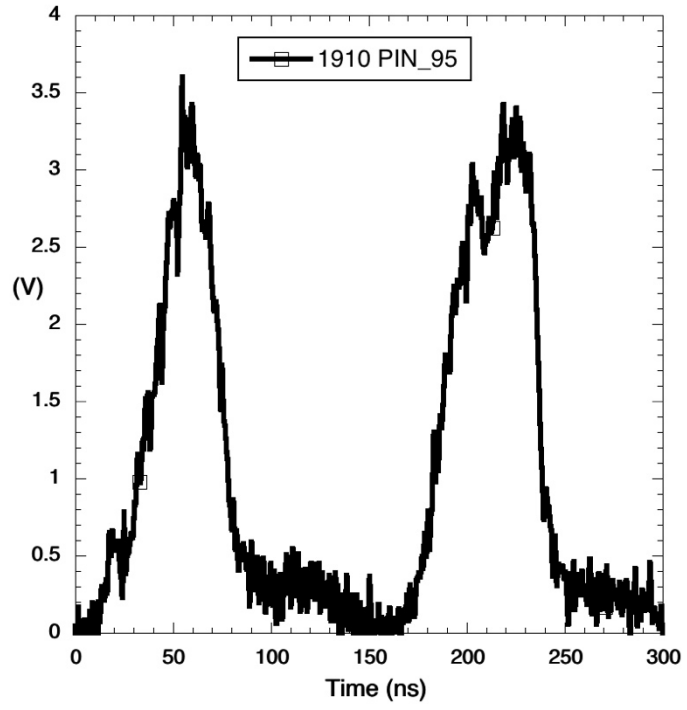


Fig. 21

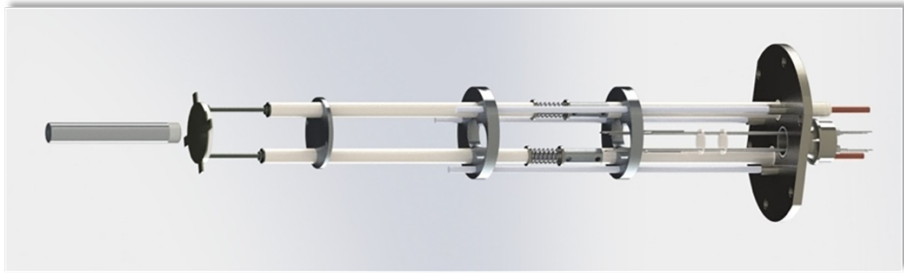


Fig. 22

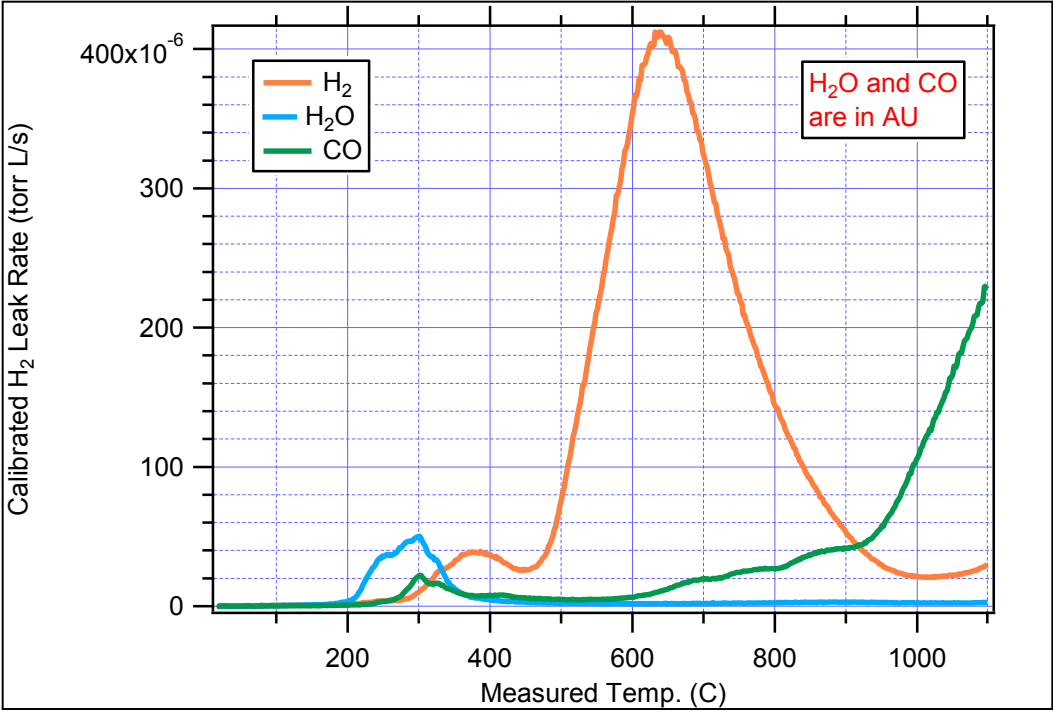


Fig. 23

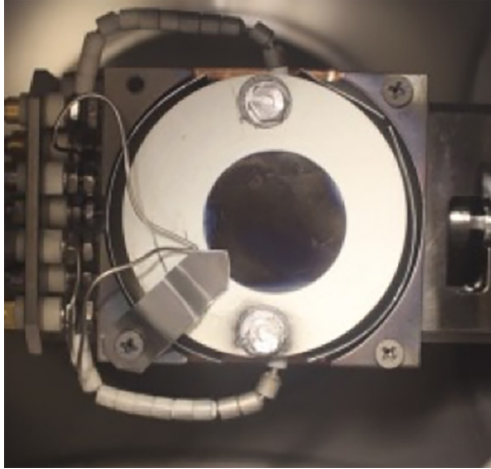


Fig. 24a

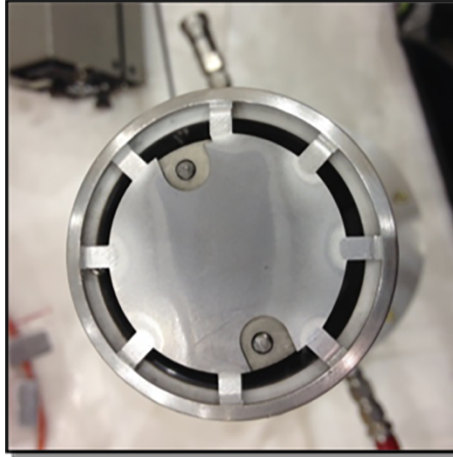


Fig. 24b

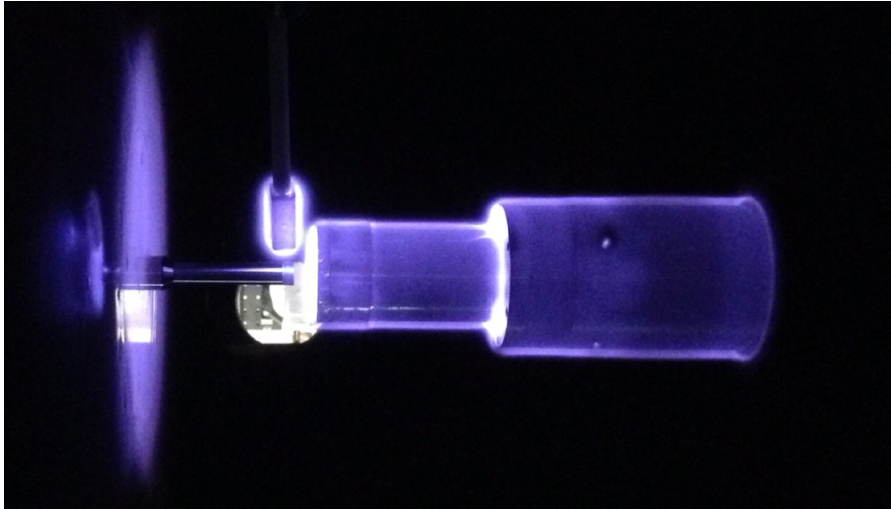


Fig. 25

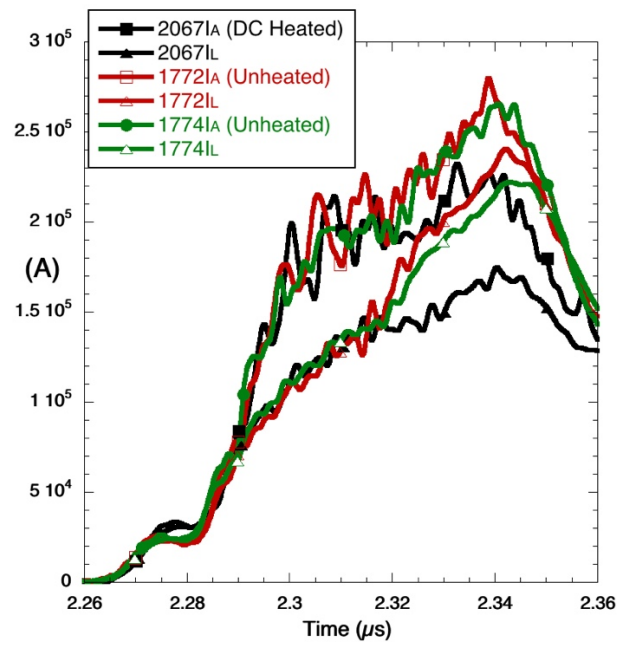


Fig. 26

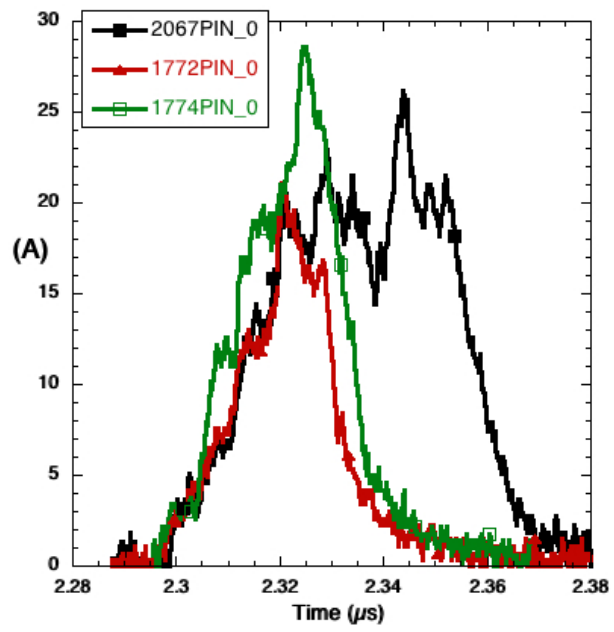


Figure 27

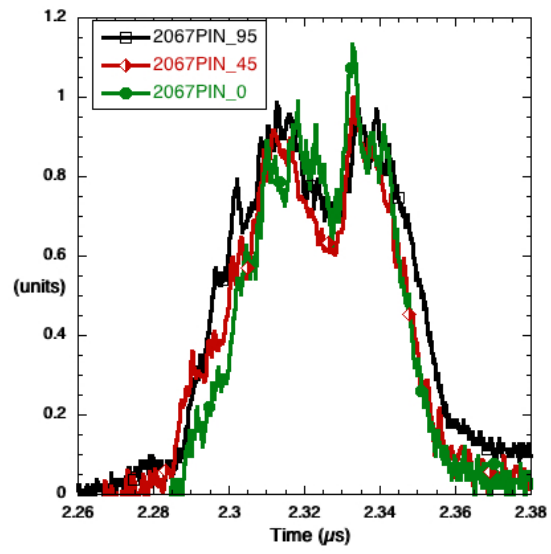


Fig. 28

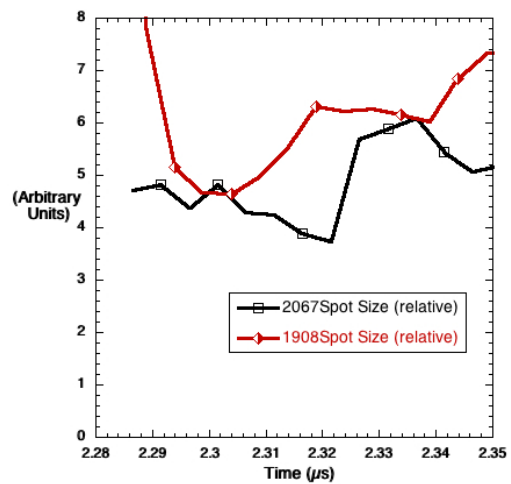


Fig. 29a

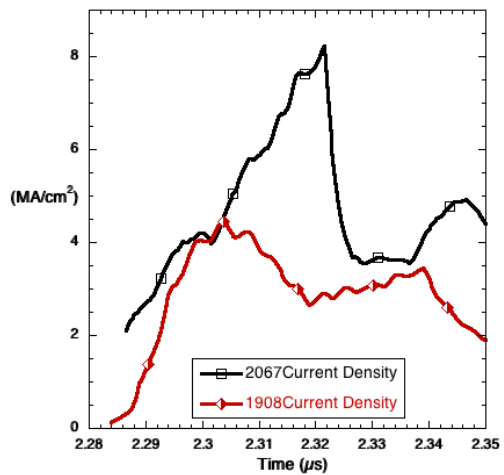


Fig. 29b